TOP-ANTITOP CROSS-SECTION MEASUREMENT STRATEGY WITH THE ATLAS DETECTOR AT THE LHC

by

Matthew Edgar LeBlanc

Thesis

submitted in partial fulfillment of

the requirements of the Degree of

Bachelor of Science with Honours in

Physics and Mathematics & Statistics.

Acadia University

May 2011

This thesis by Matthew LeBlanc

is accepted in its present form by the

Department of Physics

as satisfying the thesis requirements for the Degree of

Bachelor of Science with Honours.

Approved by the Thesis Supervisors

Dr. Anadi Canepa	Date
Dr. Svetlana Barkanova	Date

Approved by the Head of the Department

Dr. J. Craig Bennett	Date

Approved by the Honours Committee

	Date

I, Matthew LeBlanc, hereby grant permission to the University Librarian at Acadia University to provide copies of the thesis, on request, on a non-profit basis.

Signature of Author

Date

Acknowledgements

I would like to my supervisor Dr. Anadi Canepa, without whose guidance this thesis would not have been possible. I would also like to thank Dr. Ian Nugent, who wrote the framework within which my analysis was implemented, and who offered much assistance with rendering my own code functional.

Thanks as well to my internal supervisor Dr. Svetlana Barkanova and the rest of the Acadia Physics Department. In particular, I would also like to thank Dr. Michael Robertson for his constant help and wise words. Thanks are also in order for Max Turton and Nicholas Down, whose excellent instruction was a defining factor in my decision to pursue further education in science.

Thanks to both TRIUMF and the Institute for Particle Physics for not only funding this project, but also for giving me the opportunity to perform it. I would also like to thank the CERN Summer Students Programme, for providing an unparalleled environment in which to learn more than I had ever dreamt possible for one summer, and for being the catalyst of many new friendships.

Thank-you to my all of my family and friends for their help and support over the course of my degree.

Table of Contents

List of Tables

List of Figures

Abstract

A measurement of the top-antitop pair production cross-section in the dimuon channel with the ATLAS detector was made, using in a data sample of $\mathcal{L} = 32.1$ pb^{-1} from the LHC's 2010 pp collisions at $\sqrt{s} = 7$ TeV. This analysis utilizes a binned likelihood fitting algorithm to separate signal and background events. This method increases the acceptance of the signal and thus may reduce the statistical uncertainty of the measurement. The cross-section is measured to be $\sigma_{t\bar{t}} = 148.8 \pm 39.8\ (Stat.)\ \pm (Syst.)$ pb using the missing transverse energy as the discriminating variable in the fit, in agreement with the results of the ATLAS Top Physics Working Group.

Chapter 1

The Top Quark

1.1 The Standard Model of Particle Physics

The Standard Model of Particle Physics (SM) represents the culmination of understanding of the field, developed and extensively tested by the particle physics community at-large over the last thirty years. It is composed of twelve elementary particles; six quarks and six leptons, split into three distinct generations of matter. It also describes four fundamental forces and their corresponding gauge bosons which carry these interactions (see fig. 1.1). Its Lagrangian is derived from the local gauge symmetry

$$SU(3)_C \times SU(2)_L \times U(1) \tag{1.1}$$

where the three factors roughly correspond to the three interactions described by the standard model [1]: quantum chromodynamics is described by the $SU(3)$ symmetry group, and the unified electroweak force is described by the $SU(2)_L \times U(1)$ factors (with the electromagnetic and weak interactions represented by combinations of each of the two factors). These factors also describe the Higgs mechanism, which generates the masses of the fundamental particles. The Higgs mechanism is described by a scalar spin-0 boson named the Higgs boson, whose existence has yet to be confirmed experimentally.

The Standard Model has seen many triumphs in its time: it offers a compelling explanation for a wide range of experimental results, from predicting the W and Z bosons; as well as the c and t quarks to providing an explanation for the origin of both P and CP violation [2]. It also has many shortcomings: the Standard Model ignores the effects of gravitation and relativity, and fails to explain the origins of dark matter and dark energy. It assumes that neutrinos, like photons, have no mass: an assumption disproven by the results of the Sudbury Neutrino Observatory in 2001 (which are currently being reaffirmed by experiments such as the CERN-Gran Sasso neutrino beam), confirming neutrino oscillations between generations and therefore implying non-zero neutrino mass. These shortcomings do not mean that the Standard Model is a failure, but rather demonstrates why the focus of research in particle physics (and amongst LHC scientists in particular) is to find ways of refining their cornerstone; of re-tuning and re-imagining its parts in order to more thoroughly explain the world.

1.2 The Top Quark

The story of the top quark begins in 1974, as an effort to dismiss complications in the established theoretical model of hadrons due to the observation of CP-Violations in kaon decay by Christenson *et al.* [4] a decade prior. It was then that Kobayashi and Maskawa [5] suggested the possibility of a new generation of quarks would rectify theory and experiment once again. This sentiment was echoed two years later by Harari [6], who named the additional doublet of quarks as ‘top’ and ‘bottom’ in the spirit of the existing ‘up’ and ‘down’ quarks. These predictions began to gain more credibility throughout the 1970s, though the standard model contained only two pairs of quarks and two leptons during most of this time. Even

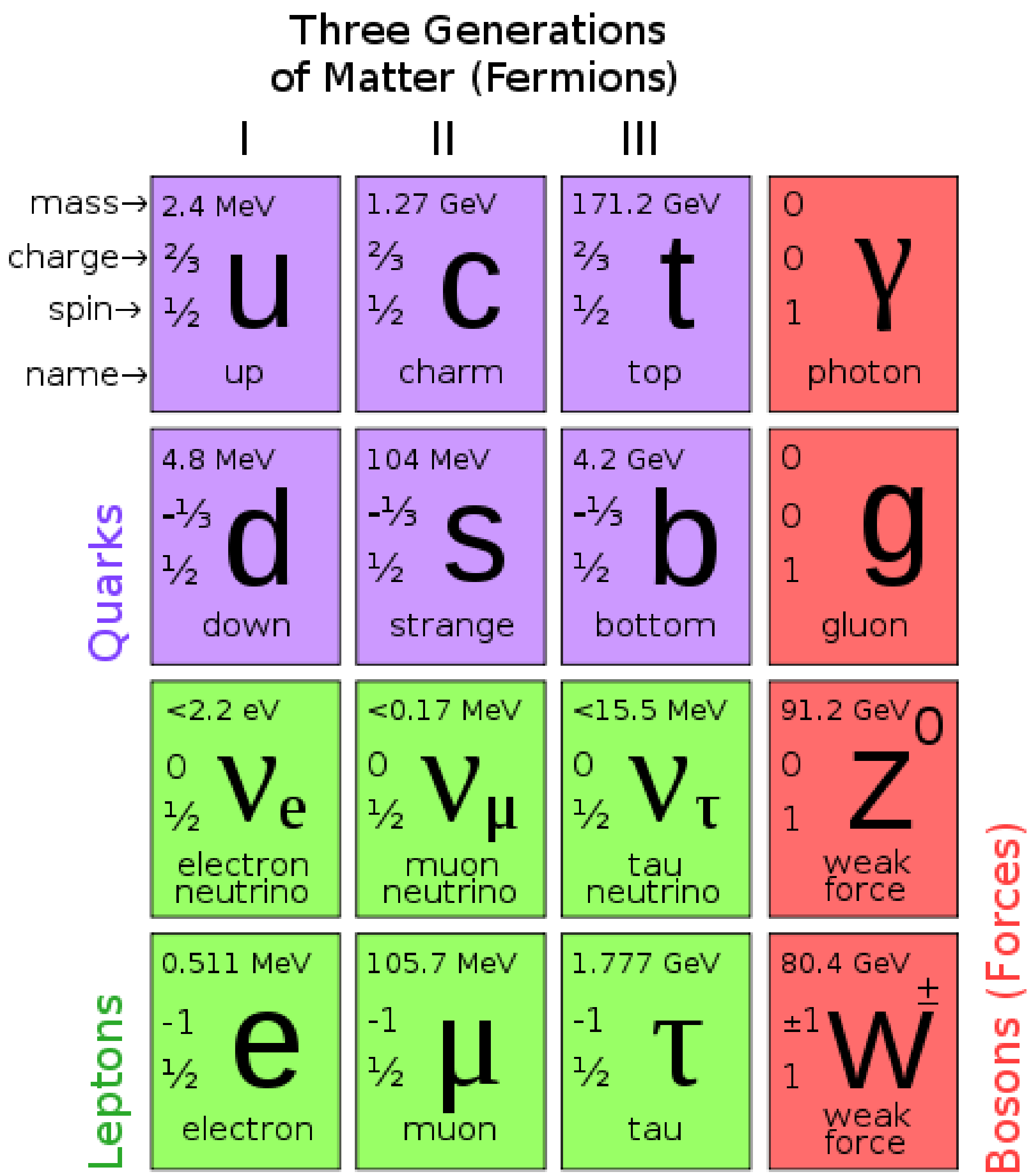

Figure 1.1: The Standard Model of Particle Physics [3].

so, it was not until the Standford Linear Accelerator (SLAC) discovered the third-generation tau lepton, under the guidance of Martin Lewis Perl in 1978 [7], that the scientific community at-large considered the exposure of a third pair of quarks to be immanent.

Confirmation of the top's existence; however, was anything but prompt. Many prominent international laboratories for particle physics joined in the hunt, but despite efforts from SLAC, DESY and CERN all efforts throughout the 1980's returned nothing but a steadily increasing lower bound on the top mass and on the energy required to generate the particle's signature. It was not until 1992 that the CDF and DØ experiments at Fermilab published their first potential top candidates, and another two years until they confidently published that the top had been discovered [8][9].

Many of the top quark's fundamental properties were studied in detail by the CDF and DØ collaborations, at energies up to the threshold of the Tevatron accelerator at Fermilab. The top is the weak isospin partner of the bottom quark. Like the up and charm quarks, it is a fermion of electric charge of $+2/3$ and a spin of $+1/2$. The top's most remarkable property, unique amongst the quarks is its large mass: measured to be 171.3 ± 1.1 GeV/c^2[10]. This is a mass-energy nearly 34 times greater than the next-to-most massive quark, the bottom (whose mass is measured to be $4.67^{+0.18}_{0.06}$ GeV/c^2[10]), and is roughly equivalent to the mass of an atom of Tungsten.

As a result of this high mass, the top exhibits several properties which the less massive quarks do not. One resultant experimental consequence is that the top has an extremely short lifespan - about 4×10^{-25}s, according to the Standard Model [11]. This is roughly an order of magnitude quicker than the average hadronization time, which means that the top tends to decay before it forms a hadron, which provides a chance to study the properties of a 'bare' quark outside of the normal environment of confinement by studying the single tops produced via electroweak interactions. Its mass lies close to the electroweak energy scale, making the top potentially connected to the electroweak symmetry breaking.

CERN's ATLAS and CMS detectors presented their first top-antitop candidate events in August 2010 at the ICHEP conference in Paris, France. While ATLAS only presented nine candidate events, it was enough to confirm the presence of top quarks finally having been produced in a locale beyond Chicago. At nominal luminosity, the LHC's rate of top production is expected to be orders of magnitude higher than Tevatron, yielding excellent statistics to study this unique particle. As such, the LHC already been nicknamed the 'top factory' by many of its researchers around the globe.

1.2.1 Production

There exist two possible methods of top quark production: top-antitop ($t\bar{t}$) pair production via the strong interaction, and single-top (t) production by way of the electroweak interaction. Top-antitop pair production occurs via two main channels[1]: either by quark-antiquark annihilation as $q\bar{q} \rightarrow t\bar{t}$, or through gluon fusion as $gg \rightarrow t\bar{t}$. At LHC energies, the gluon-fusion channel accounts for nearly 85% of events, and $q\bar{q}$ annihilation the other 15% (These interactions are illustrated to leading order in figure 1.2). These percentages are the opposite of those found at the Tevatron, where $q\bar{q}$ annihilation accounted for most of the top production due to increased 'gluon luminosity' at the LHC: at higher energies, a proton is much more likely to contain more gluons.

Single-top production occurs as a result of the charged-current electroweak interaction, connecting the top to the down-type quarks with coupling amplitudes

[1] A third leading-order channel, due to double-gluon splitting (fig. 1.2c), offers a negligible contribution.

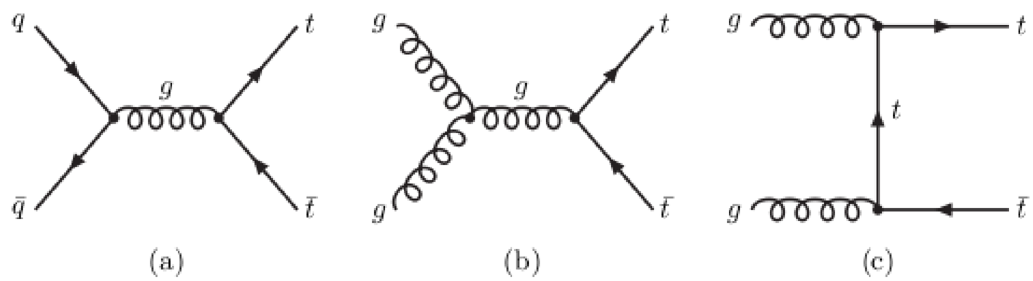

Figure 1.2: Leading-order Feynman diagrams illustrating the three top-antitop pair production channels, specifically through (a) quark-antiquark annihilation, (b) gluon fusion, and (c) double-gluon splitting [11].

proportional to the Cabbibo-Kobayashi-Maskawa (CKM) mixing matrix elements V_{tq} $(q = d, s, b)$. The three electroweak processes by which single tops may be produced are illustrated in figure 1.3: either by a virtual s-channel W (fig.1.3(a)), a t-channel W-gluon fusion process (fig. 1.3(b)) or the associated-production channel in which an on-shell W is produced alongside the t. The cross-section for each of these processes is proportional to the CKM element $|V_{tb}|^2$, and as such measuring each of these individual cross sections allow direct methods of measuring this parameter.

1.2.2 Decay

According to the Standard Model, a top quark will decay as $t \to Wb$ in more than 99.8% of cases, after which the W will decay either as $W \to \ell\nu$ or $W \to q\bar{q}$, as shown in figure 1.4. The only other leading order decays permitted in the Standard Model are $t \to Ws$ and $t \to Wd$, but both channels have low branching ratios and have low experimental sensitivity. Other SM decay modes exist at higher orders of perturbation theory via other processes such as flavour-changing neutral currents, with branching ratios $\mathcal{O}(10^{-13})$. The probabilities of these decay modes are predicted to be higher by certain models of physics beyond the SM, such as MSSM and various technicolour theories.

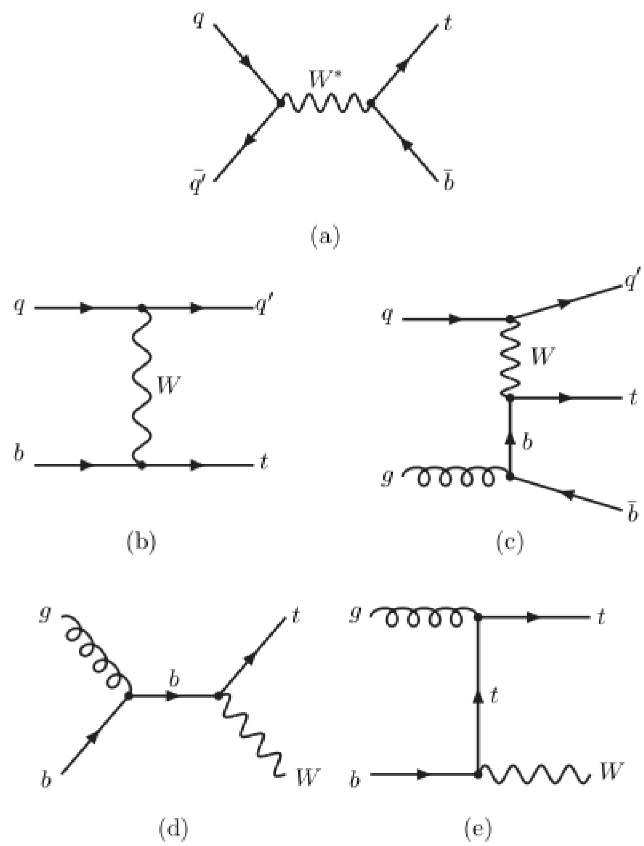

Figure 1.3: Leading-order Feynman diagrams illustrating single-top production via the electroweak interaction, in the (a) s-channel, (b,c) t-channel, and (d,e) W channel [11].

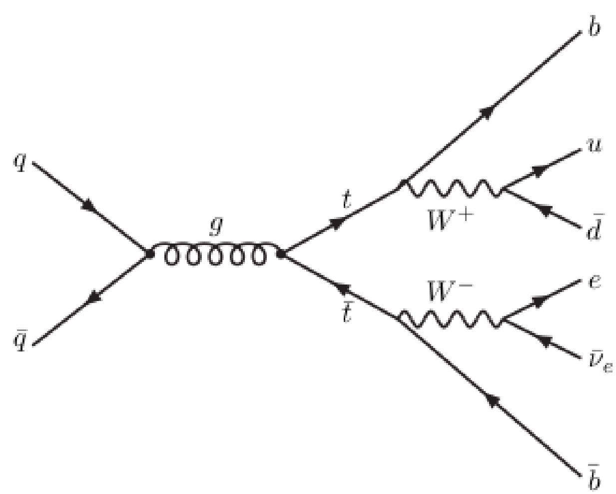

Figure 1.4: A standard top-antitop decay Feynman diagram illustrating the single lepton channel [11].

1.2.3 Cross Section

One of the most crucial observable parameters to measure is the cross-section of the $t\bar{t}$ interaction, the probability that a pair of top quarks is produced in any given pp collision. It may be expressed as:

$$\sigma_{t\bar{t}} = \frac{N_{Obs} - N_{Bg}}{\varepsilon \cdot \mathcal{L}} \tag{1.2}$$

where σ is the cross-section itself; N_{Obs} and N_{Bg} are the number of signal and background events detected; ϵ is the detector efficiency and $\mathcal{L}$ the integrated luminosity of the data sample being examined. A rough idea of the associated uncertainty in this measurement is described by standard error propagation methods in equation 1.3, and offers some guidance to consider when attempting to make a more precise cross-section measurement:

$$\frac{\Delta\sigma}{\sigma} = \sqrt{\frac{\Delta N_{obs}^2 + \Delta N_{bg}^2}{(N_{obs} - N_{bg})^2} + \left(\frac{\Delta\mathcal{L}}{\mathcal{L}}\right)^2 + \left(\frac{\Delta\varepsilon}{\varepsilon}\right)^2} \tag{1.3}$$

In the 'cut-and-count' analysis carried out by the ATLAS Top Working Group on 35.3 pb^{-1} of data collected during the 7 TeV run in 2010 [12], a minimum threshold cut will be defined on certain kinematic variables and events which do not meet this threshold are not considered in the analysis (this method, along with these minimum event selection criteria are defined in detail in chapter 3). This type of analysis may result in acceptance losses, which is not in itself an issue when performing an analysis with normal statistics.

As the main focus of this thesis, an alternative method of measuring the $t\bar{t}$ cross-section is examined that hopes to maximize the event acceptance by using less restrictive event selection criteria than that defined for standard 'cut-and-count' methods. A binned-likelihood fitting technique (which uses the shapes of the kinematic signal and background observables) will be employed to extract the number of $t\bar{t}$ signal and background events present in the LHC 2010-7 TeV dataset. This preliminary study has focussed on measuring the $t\bar{t}$ cross-section in the dimuon channel due to relatively low backgrounds when compared to the other decay modes, in an effort to validate this approach before it is more broadly applied.

1.2.4 A Window to New Physics

The top quark represents an excellent tool in the modern particle physicist's kit with which to observe new phenomena beyond the physics of the Standard Model. Studying their production rates and characteristics provides a sensitive probe which may reveal discrepancies between experiment and standard model predictions, paving the way to new discoveries.

According to the Standard Model, all possible top decay modes other than $t \to Wb$ are highly suppressed, resulting in a branching ratio $\Gamma_{t\to Wb} \approx 1$. Certain models of BSM physics - most notably minimal supersymmetry (MSSM), variants of technicolour theory, and models with additional generations of quarks - introduce flavour-changing neutral currents which increase the $t \to gc$ and $t \to \gamma c$ branching ratios [13][14], revealing one promising place to observe deviations from the standard model.

The production of non-SM particles may also be detected by examining top decays. In composite Higgs models as well as supersymmetric models, charged Higgs bosons may be produced though the decay channel $t \to H^+ b$. The H^+ typically decays in one of two channels: primarily as $H^+ \to \tau\nu$ or else hadronically as $H^+ \to \bar{c}s$. By searching for a decay rate of ts into τs inconsistent with the SM for the first case or for hadronic t decays which exhibit kinematics inconsistent with $W \to q\bar{q}$, these forms of new physics could also be detected [13][14].

Measurements of the top quark mass also help indirectly pin down the allowed range of masses for the ever-elusive Higgs boson. Due to the large value of the top mass, it contributes to the electroweak radiative corrections of the W boson. Precisely measuring the top and W masses allows an estimate of the Higgs mass to be made [14]. The result of this analysis, performed by Fermilab's CDF and D0 collaborations, as well as CERN's LEP Electroweak Working-Group, are shown in figure 1.5. This plot illustrates the range of possible Higgs masses (the shaded green regions) as a function of the top and W masses. Also shown are a pair of ellipses, which denote the regions with mass values for the top and W permitted by the LEP and Tevatron experiments. The region where both ellipses overlap with the green shaded region indicates the preferred Higgs mass [15].

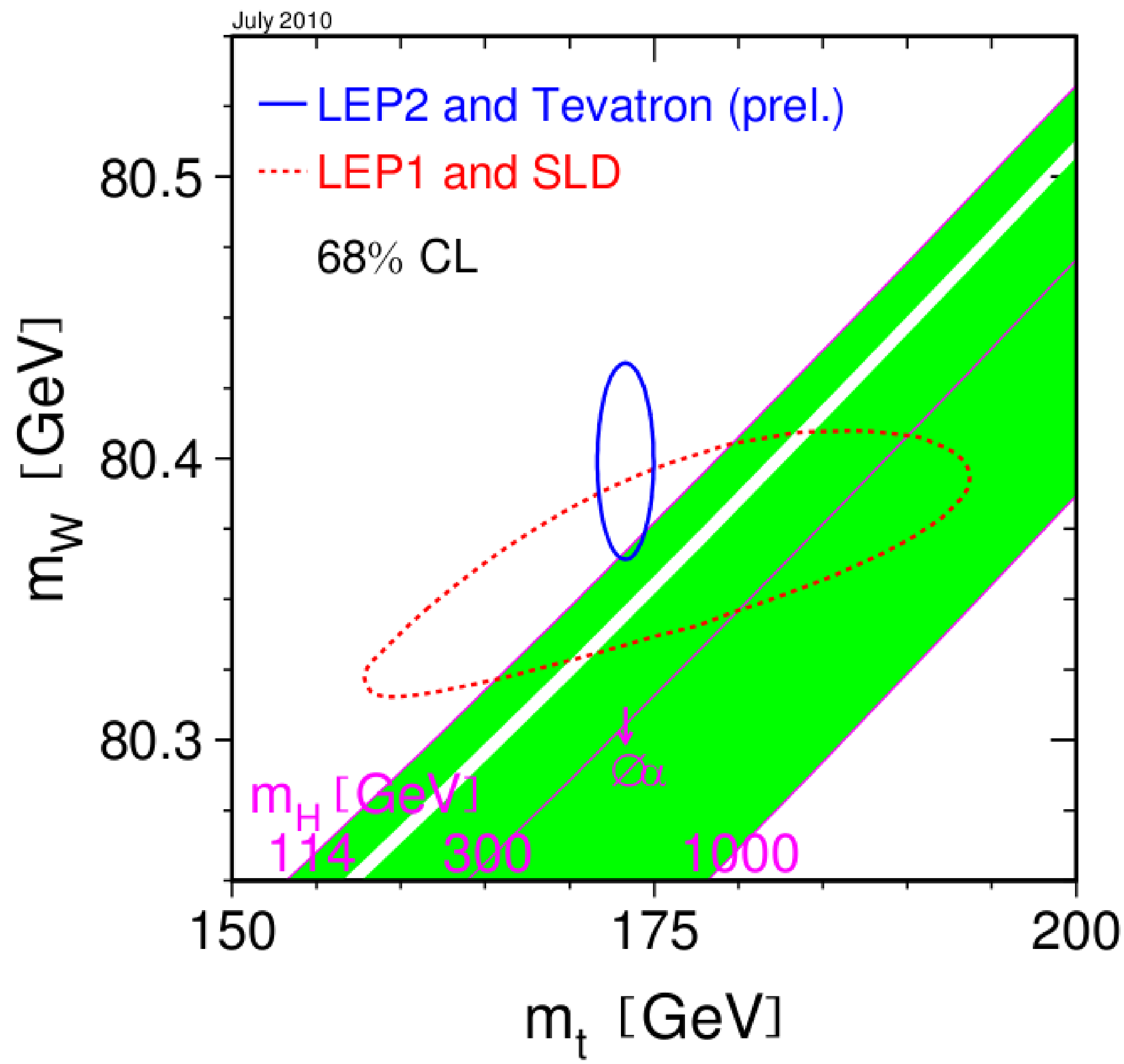

Figure 1.5: A plot illustrating the range of possible Higgs masses (the shaded green regions) as a function of the top and W masses. Also shown are a pair of ellipses, which denote the regions with mass values for the top and W permitted by the LEP and Tevatron experiments. The region where both ellipses overlap with the green shaded region indicates the preferred Higgs mass [15].

Chapter 2

The Large Hadron Collider and the ATLAS Detector

2.1 The Large Hadron Collider

The Large Hadron Collider (LHC) was conceived, designed and built with a single goal in mind: "to reveal the physics beyond the Standard Model with centre of mass collision energies of up to 14 TeV" [16].

The machine resides in a circular tunnel with 27km circumference, 100m below the European Organization for Nuclear Research (CERN) and nearby French and Swiss countrysides. It represents one of the single largest scientific undertakings in history since the space race, and is the result of the collaboration of over ten thousand scientists from more than one hundred different countries, over the course of more than a decade of planning and construction.

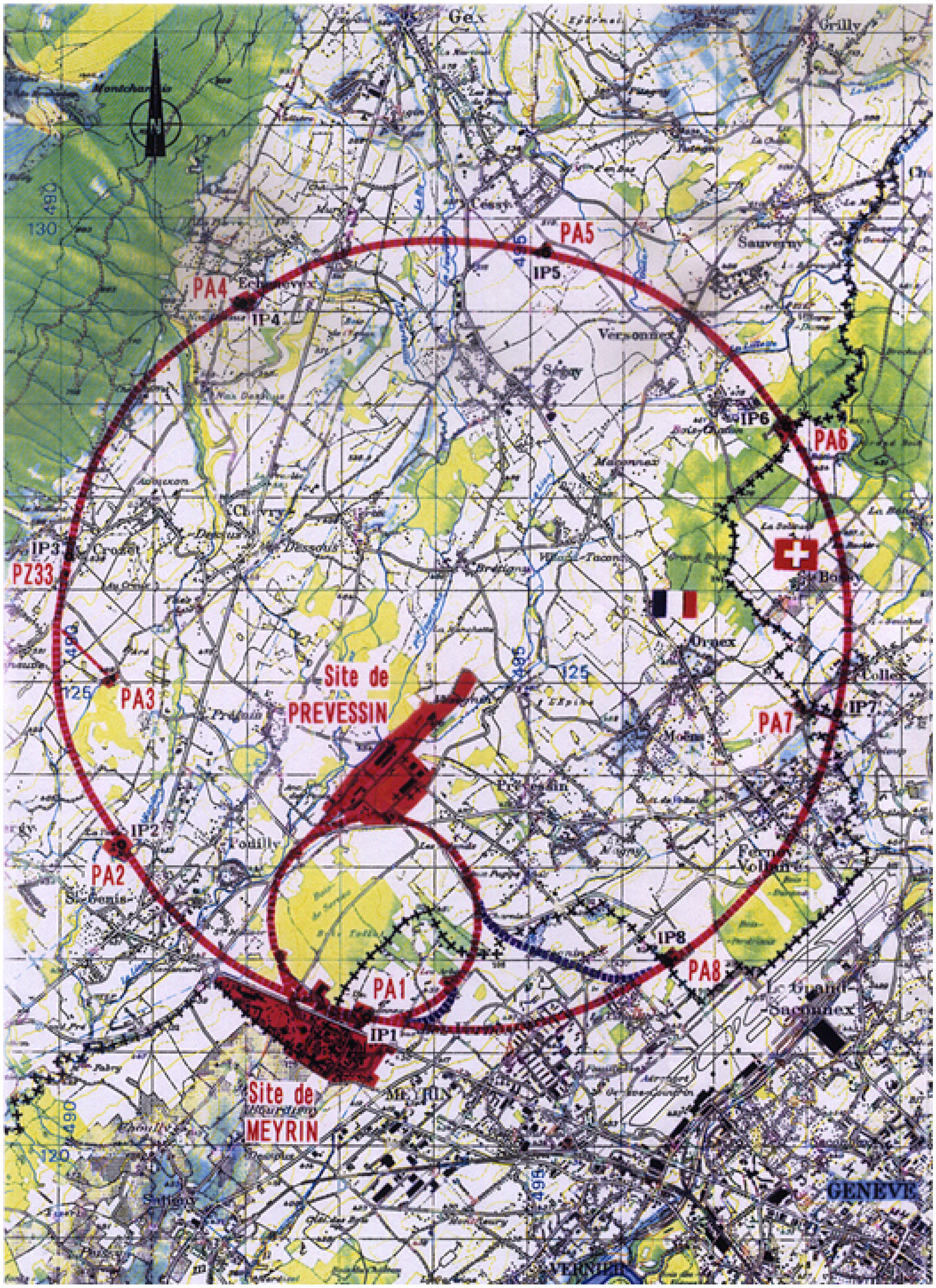

Figure 2.1: A map of the greater Geneva region, outlining the location of the CERN Meyrin and Prevessin sites, as well as the LHC ring. The ATLAS detector is located at the site labelled PA1 [17].

The LHC is a proton-proton synchrotron, built to accelerate protons and lead nuclei up to centre-of-mass energies of $\sqrt{s} = 14$ TeV[1]. Particle beams are accelerated in the CERN super proton-synchrotron (SPS), and fed into the LHC tunnel in opposite directions. The beams are then made to collide at one of four experimental sites located at points PA1 (ATLAS), PA2 (ALICE), PA5 (CMS), and PA8 (LHCb) along the ring, as shown in figure 2.1.

The LHC beams are accelerated and stabilized by a lattice of 1232 15m-long superconducting dipole magnets used to bend the beam, and 392 5-7m long superconducting quadrupole magnets used to focus it. The proton beams are not continuous; rather each is composed of proton 'bunches' nominally containing 1.15×10^{11} protons per bunch. Bunches are nominally grouped in sets of 3 and 4 in the sequence

334 334 334 333

and injected until 2808 bunches fill the machine with a spacing of 25ns between bunches, resulting in an average bunch crossing rate of 31.6 MHz [18]. The missing bunch at the end of each fill sequence is known as the 'abort gap'. These gaps allow adequate time for the beam-dump kicker magnets to ramp up their electrical current in the case of a sudden dump, allowing the beam to be extracted safely without risking damage to the tunnel or detectors.

The **Instantaneous Luminosity**, or particle flux, is defined to be the number of particles which pass through one unit area, per each unit of time. For a pair of directly opposed relativistic beams such as those used inside of the LHC, the luminosity is given by

$$L = fn\frac{N_1 N_2}{A} \tag{2.1}$$

[1]Over the course of data collection in 2009-2010, the LHC is operating at half-nominal centre-of-mass energy; $\sqrt{s} = 7$ TeV

where N_1 and N_2 are the number of particles in each bunch, n is the number of bunches in either beam, A is the cross-sectional area of the beam and f is the revolution frequency (nominally 40 MHz in the LHC). This quantity is directly related to the amount of data delivered by the detector, conventionally reported as the **Integrated Luminosity**. Over the course of its first set of pp collisions, ATLAS recorded $\mathcal{L}$ =45.03 pb^{-1} of physics data.

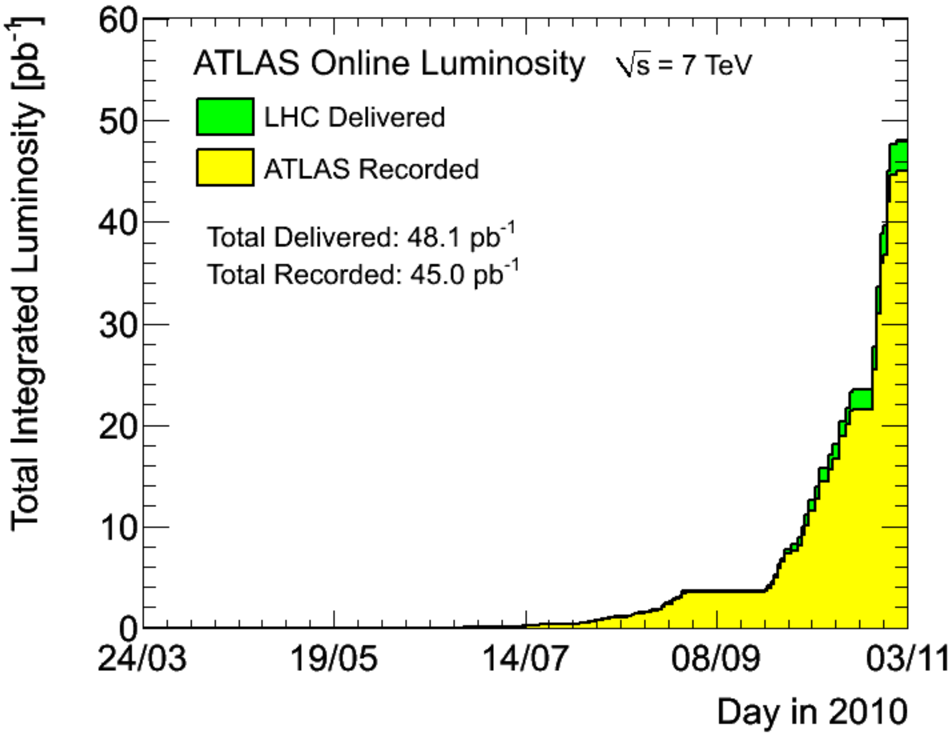

Figure 2.2: A plot of integrated luminosity delivered to-date by the LHC pp collisions as of November 5th, 2010 [19].

2.2 ATLAS

The ATLAS (**A** **T**oroidal **L**HC **A**pparatu**S**) detector is the largest of four experiments currently installed in the Large Hadron Collider (LHC) at CERN. It was designed and built as a general-purpose detector, intended both for taking precision measurements of known processes as well as maintaining a wide scope for discovering new physics.

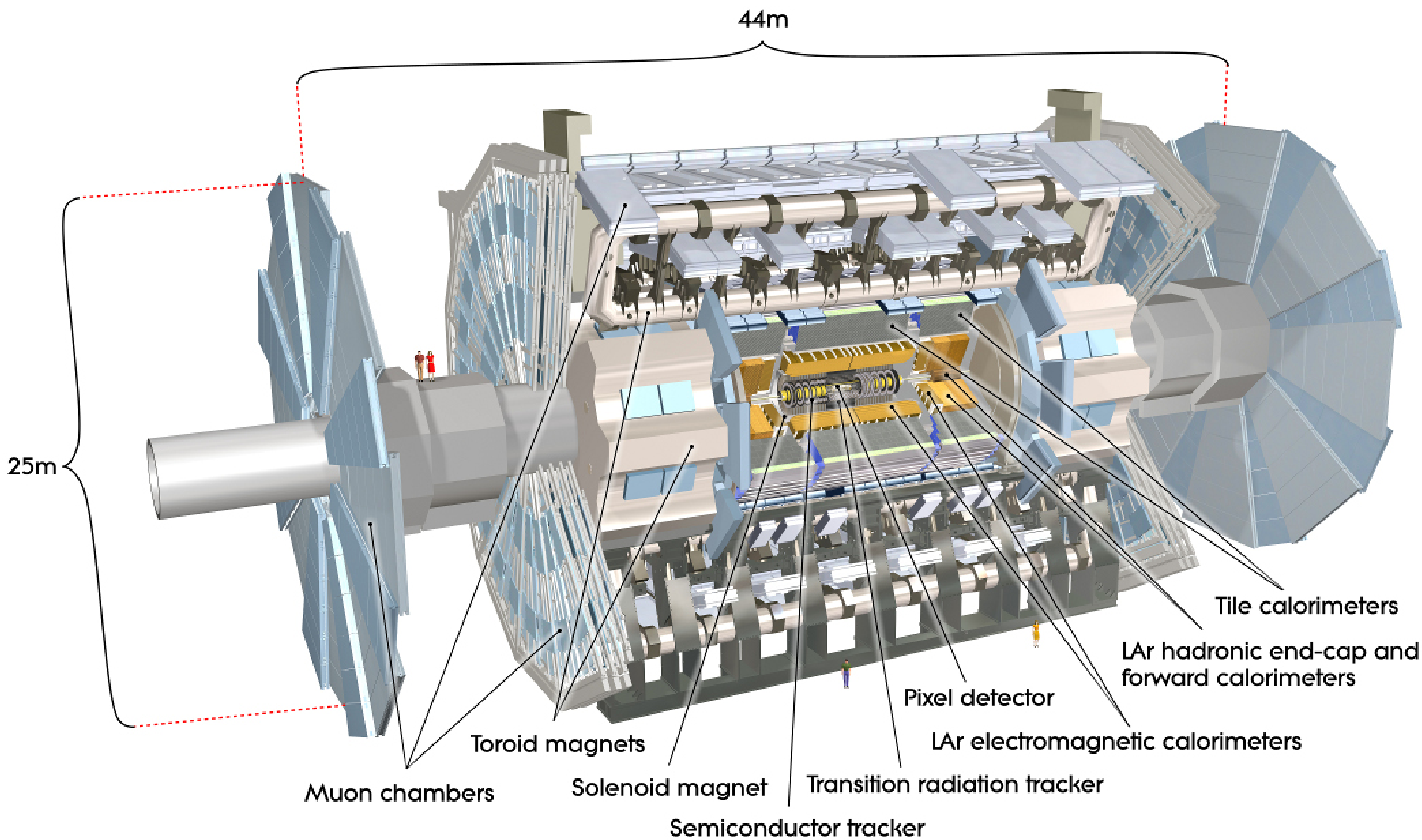

Figure 2.3: The ATLAS detector. Altogether, the detector is 44m long and 25m in diameter, and weighs nearly 7000 tons [20].

2.2.1 Coordinate System

The conventional, right-handed coordinate system used in most ATLAS physics discussions is defined as-follows [16]:

- The origin is defined to be the location of the primary interaction, or beam-crossing.
- The z-direction is defined along the beam axis, with positive z in the direction of ATLAS's side A (facing east, towards Geneva), and negative z in the direction of ATLAS's side C (facing west, towards the French Jura region). The $x - y$ plane is transverse to the beam.
- The positive x-direction points towards the centre of the LHC ring. The positive y-direction points upwards, toward the ceiling of the ATLAS cavern[2].
- The azimuthal angle ϕ is measured conventionally, with $\phi = 0$ in the positive direction and sweeping around the beam.
- The polar angle θ is defined in the $x - z$ plane, with $\theta = 0$ along the positive z-direction.
- The pseudorapidity η provides a convenient coordinate system in which the difference in rapidity of any two particles is independent of the boost. It is defined such that

$$\eta = -\ln\left(\tan\frac{\theta}{2}\right). \tag{2.2}$$

[2]The positive y direction is in fact defined as 0.704 degrees off of true vertical, due to the general tilt of the LHC tunnel [21].

2.2.2 Inner Detector

ATLAS's inner detector is designed to give precision measurements of particle position and momentum. The barrel detectors reside entirely within the main barrel solenoid magnet at distances as close as 5cm from the interaction point. The inner detector measures 7m long with an outer radius at 1.15m from the interaction point, and consists of three major parts, illustrated in figure 2.4:

- The **pixel detector** takes measurements over the full detector acceptance range with extremely high granularity, as closely to the interaction point as possible: from 5cm to 12cm away via over 80 million pixels [22]. Typically, three pixels are activated by each particle track. The pixel detector plays a major role in locating secondary vertices from particles created by the initial *pp* collision.

- The **semiconductor tracker (SCT)** consists of 8 layers of silicon strip detectors wrapped around the pixel detector. The silicon detectors each measure 6.31cm $\times$ 6.4cm and provide 780 separate readout channels [22]. The SCT provides an additional 8 measurements per particle track in the detector, aiding in measuring the momentum of charged particles curving in the solenoid field.

- The **transition radiation detector (TRT)** is a traditional straw-tube detector made of straw tubes filled with xenon gas surrounding a gold-plated tungsten-rhenium wire. There are 50 000 straws in the detector barrel (each providing two readout channels), and 320 000 straws in the end caps (each providing one) [22] which together add an average of 35 hits to $2 > \eta > 2.7$ a particle track. This detector is capable of operating at high rates and provides the last layer of tracking data before particles enter the calorimeter systems.

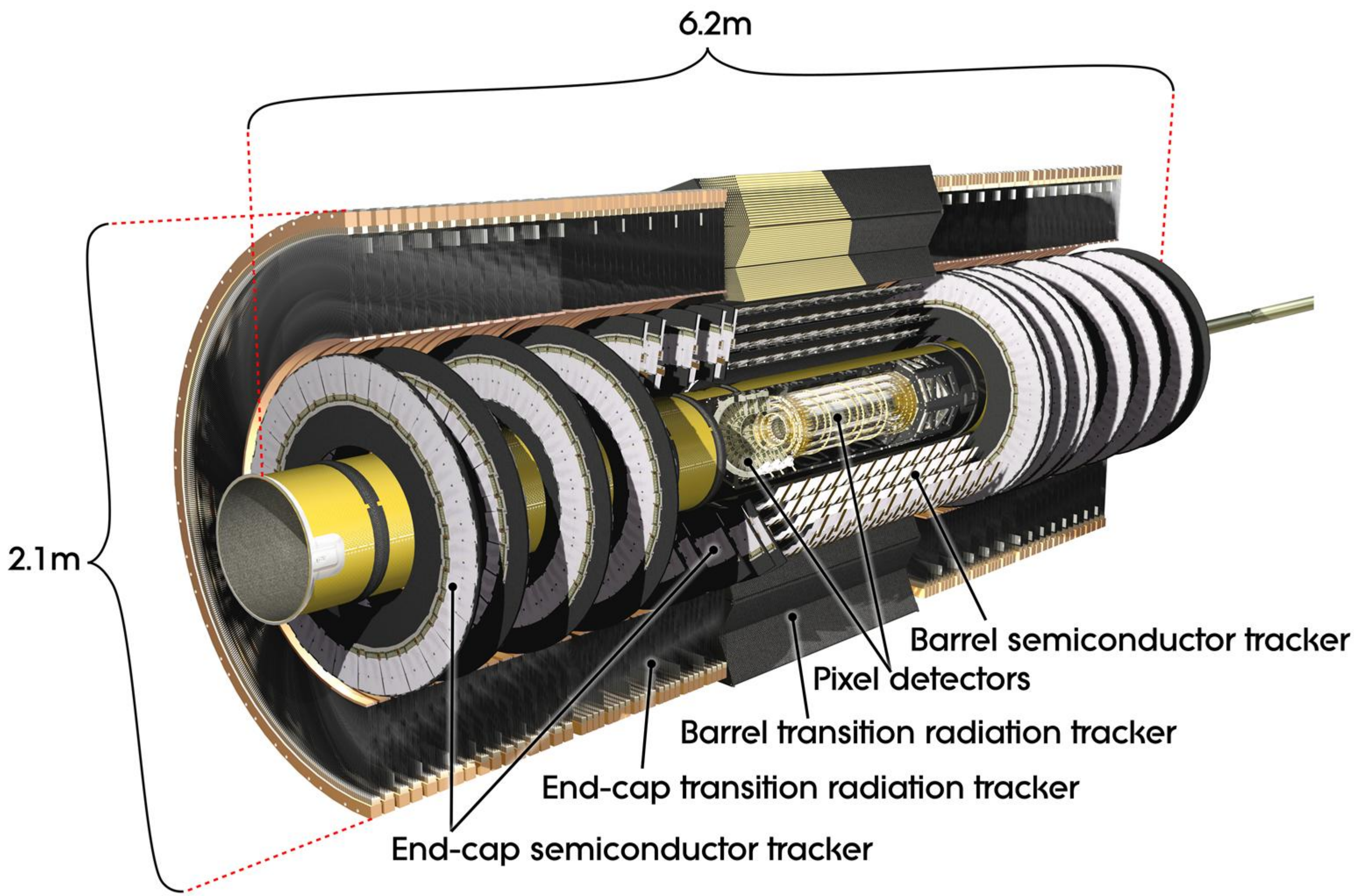

Figure 2.4: The ATLAS inner detector, denoting the locations of the pixel, SCT and TRT straw-tube tracking systems [23].

2.2.3 Calorimeters

The goal of a calorimetry system is twofold: to provide measurements of how much energy incident particles posses, as well as to report the location of the energy deposit.

ATLAS's electromagnetic and hadronic calorimeters are constructed quite differently, though they both share the same underlying concepts: in each, an active ionizing material is surrounded by sets of electrodes. As particles originating from the collision pass through the calorimeter, they ionize the active layer and cause a shower of charged particles to be pulled towards and strike the electrodes. By digitally monitoring the electrodes, values of the location and magnitude of energy deposited by the particles measured.

Calorimeter depth is an important consideration in detector design: ideally, the calorimeters would be deep enough that every particle passing through deposited the entirety of their energy inside; however, for practical reasons this is not possible. The electromagnetic calorimeter was designed to provide optimal containment for particles interacting electromagnetically with the detector in order to prevent spillover into the hadronic calorimeter, which could result in the mis-identification of electrons as jets. Its depth is measured in radiation lengths (X_0), defined to be the distance an electron must travel in the calorimeter to have its energy reduced by a factor of $1/e$. The depth of the hadronic calorimeter is conventionally measured in terms of interaction lengths (λ), as the average distance a particle travels without interacting elastically or quasi-elastically. Likewise, it was necessary that the hadronic calorimeter contain all interacting particles except for muons, without allowing spillover to the muon systems.

Calorimeter resolution is defined as the ratio between the measured energy of an object and its true energy, divided by the true value.

$$Resolution = \frac{E_{measured} - E_{true}}{E_{true}} \tag{2.3}$$

The resolution represents a quantification of the accuracy of the calorimeter, which is optimal when made as small as possible.

Electromagnetic Calorimeter

The electromagnetic (EM) calorimeter is the detector's innermost calorimetry system, tasked with measuring the energy of particles producing EM showers (photons and electrons) produced as a result of the LHC's proton-proton collisions.

The electromagnetic calorimeter (visible in figure 2.5) uses a lead-liquid argon design and is composed of two end-cap calorimeters, which span the pseudorapidity range $1.375 < |\eta| < 3.2$ and a single barrel calorimeter, which spans $0 < |\eta| < 1.475$. In the barrel, the absorbers are accordion-shaped in order to fit seamlessly together with constant gap thickness when installed, as well as to minimize induction along signal paths during readout (a significant consideration when recording events at intervals of 25 ns [25]). The end-cap calorimeters are constructed similarly, instead with absorbers arranged radially as spokes in a wheel with varying gap thickness.

The depth of the electromagnetic calorimeter is > 22 radiation lengths (X_0) in the barrel ($24X_0$ in the end-caps). Between the barrel and end-cap calorimeters, the electromagnetic calorimeter contains over 163 968 readout channels for data-taking and possesses an energy resolution of $10\%/\sqrt{E} + 0.7\%$.

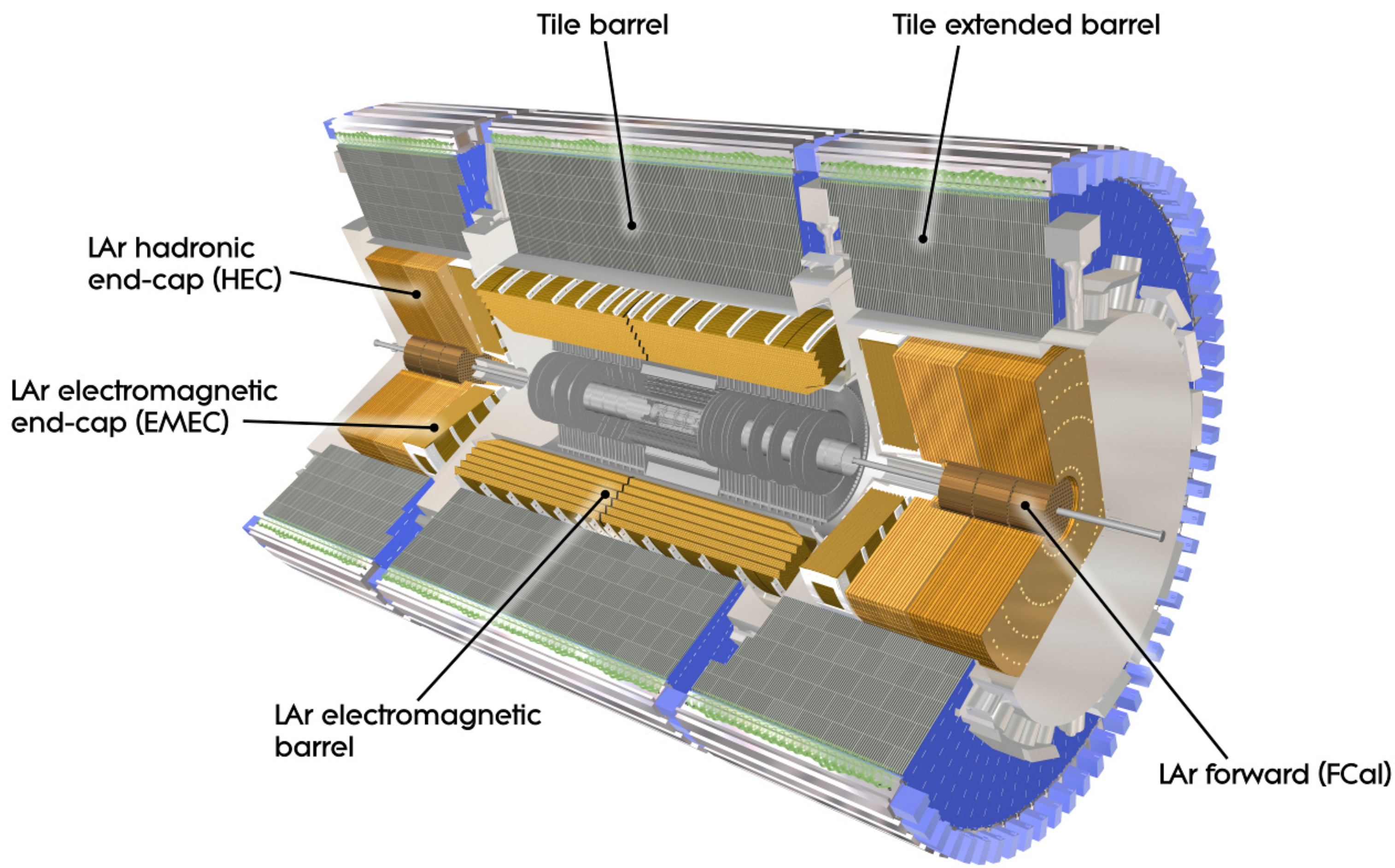

Figure 2.5: The ATLAS detector's calorimetry systems. The electromagnetic barrel and end-cap calorimeters, as well as the hadronic HEC, FCal and tile calorimeters are illustrated [24].

Hadronic Calorimeters

The energy of particles passing through the calorimetry system can also be measured via their hadronic processes. ATLAS accomplishes this by using a set of three principal hadronic calorimeters:

- The **Tile Calorimeter** (visible in figure 2.5), which surrounds the electromagnetic barrel calorimeter over the pseudorapidity range $|\eta| < 1.7$, consists of three layers of a steel absorbing material coated with scintillating tiles. It extends outward radially through the range 2.8 m$< r <$ 4.25 m and ranges between 1.5-1.8 λ thick in the inner-barrel and 1.5-3.3 λ thick in the extended-barrel portions. The tile calorimeter contains 9 852 readout channels with an η vs. ϕ segmentation of 0.1×0.1 in the inner two sections and 0.1×0.2 in the outermost, providing an energy resolution of $50\%\sqrt{E} + 3\%$ [26].

- The **LAr Hadronic End-cap Calorimeter** (HEC) (shown in figure 2.5 and more closely in figure 2.6) extends the system through $|\eta| < 3.2$. It consists of copper plates, with interleaved 8.5 mm LAr gaps as the active medium, and possesses an energy resolution of $20\% - 60\%/\sqrt{E} + 0.3\% - 10\%$. As a point of interest, the HEC marks one of the Canadian contributions to the construction of the ATLAS detector, and was largely designed and constructed by scientists at Vancouver's TRIUMF laboratory [27].

- The **LAr Forward Calorimeter** (FCal) is itself composed of three sections (as shown in figures 2.5 and 2.6): the first, with a copper absorption medium, measures electromagnetic deposits in this region close to the beam direction. The other two, which instead use tungsten, are optimized in order to collect readings of hadronic energy deposit with a resolution of $100\%/\sqrt{E} + 10\%$. All sections use a straw-detector design, wherein small wires of absorption material are laid densely packed together (with gaps as small as 0.25 mm in some regions), parallel to the beam direction. The FCal is roughly 10 λ deep and contains 3 524 readout channels. In all cases, liquid argon is used as the active ionizing medium. The FCal was another Canadian contribution to the construction of the ATLAS detector, and was largely constructed at the University of Toronto and Carleton University.

2.2.4 Muon System

ATLAS's muon spectrometers represent a cornerstone of the detector's analysis strategy, and extend from the outside of the hadronic calorimeter at $r = 4.5$ m to the outer edge of the detector at $r = 11$ m. The spectrometer detection system (shown in figure 2.7) consists of monitored drift-tube trackers within ($|\eta| < 2.7$), except in the innermost chamber, which instead employs cathode strip chambers ($2 < |\eta| < 2.7$). Altogether, these chambers possess nearly one million readout channels. The muon LV1 trigger resides in the resistive plate chambers covering the pseudorapidity range $|\eta| < 1.05$ and in the thin-gap chambers in the range $1.05 < |\eta| < 2.7$.

The other major components of the muon systems are the large, toroidal air-core superconducting barrel magnets from which the detector derives its name. These magnets, along with the pair of end-cap toroids placed at either end of the detector, bend incident muons in the plane orthogonal to their trajectory. This type of bending allows the momentum of the muons to be found with high precision, facilitating the discovery-physics analysis ATLAS was designed to perform: for 1 TeV muons, this means an energy resolution of $\sigma p_T / p_T = 10\%$.

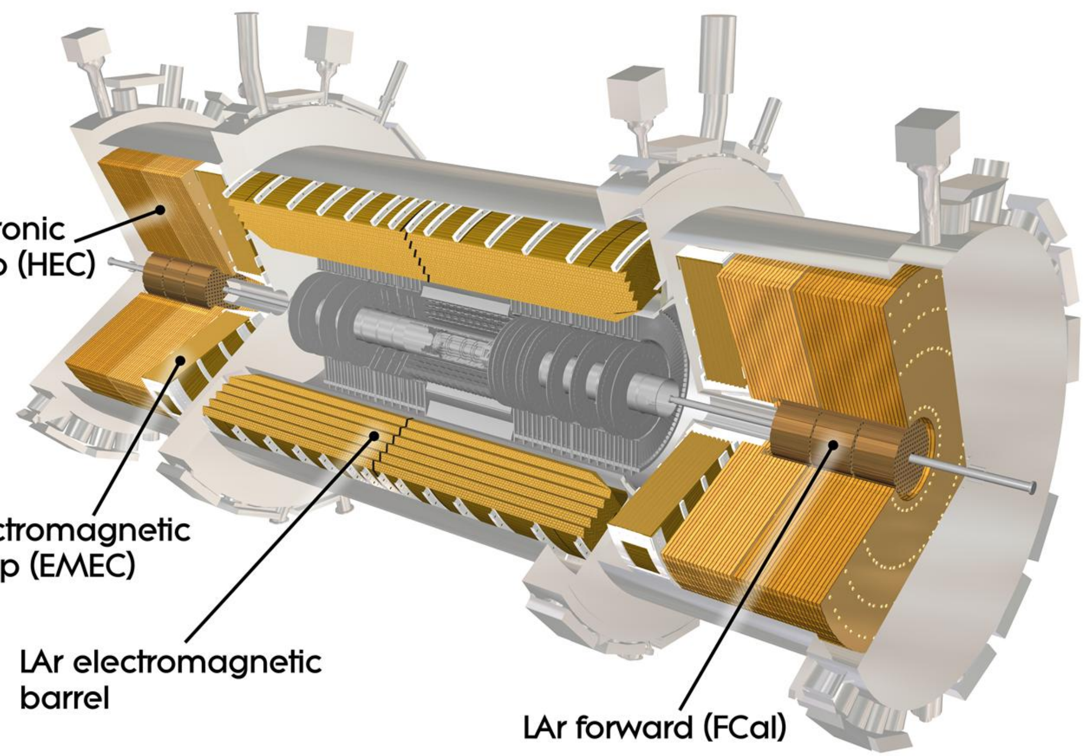

Figure 2.6: The ATLAS detector's liquid argon calorimetry systems. The LAr hadronic endcap (HEC), electromagnetic endcap (EMEC), electromagnetic barrel and forward calorimeters are denoted [28]. The LAr calorimetry systems represent a major area of Canadian contribution to the ATLAS collaboration, as both major portions of the HEC and FCal were designed, constructed and tested at Canadian institutions (TRIUMF and the University of Toronto, respectively).

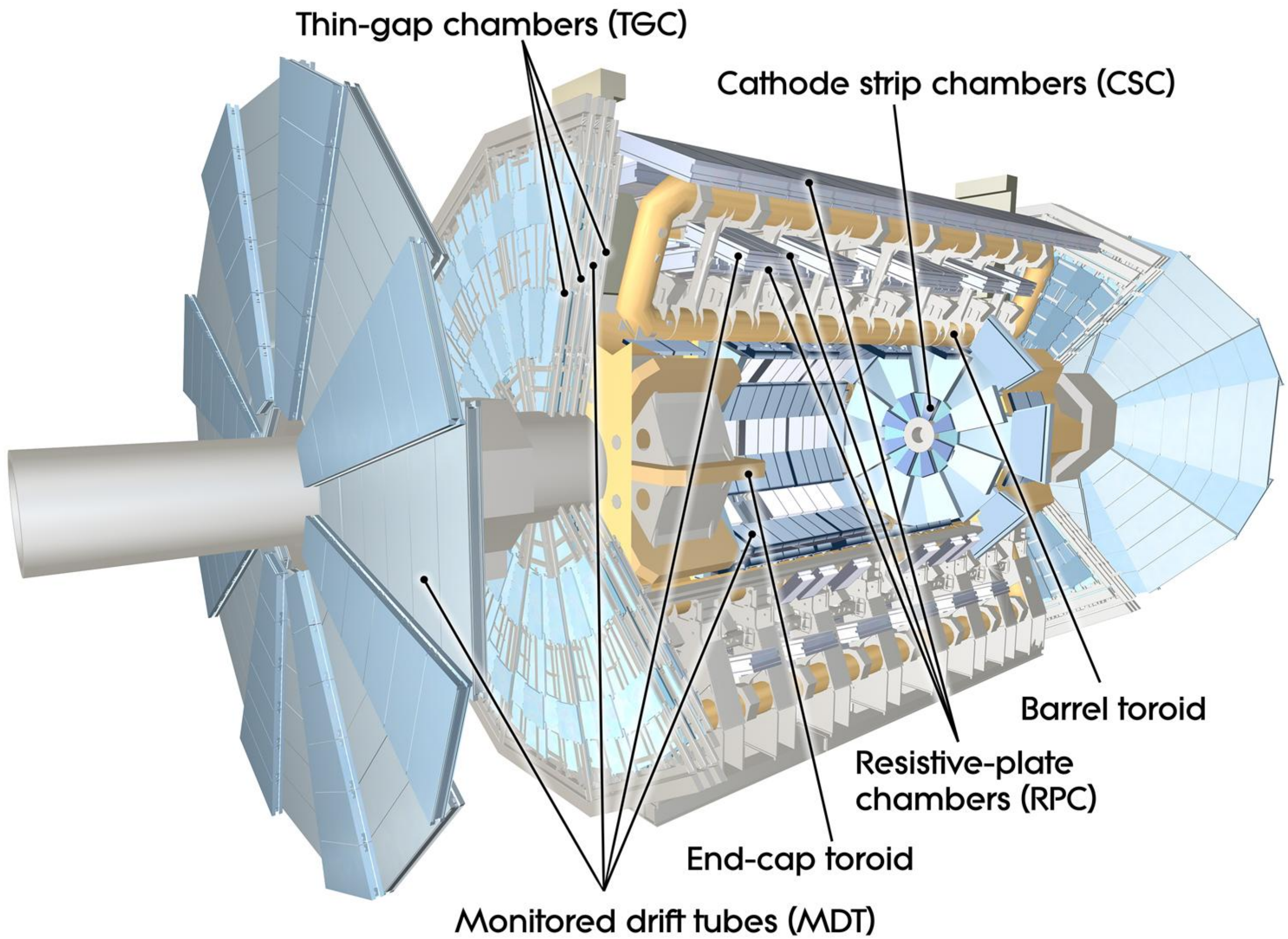

Figure 2.7: The ATLAS detector's muon systems, showing the barrel toroid magnets [29].

2.2.5 Trigger

At nominal instantaneous luminosities, the LHC will produce about six hundred million collisions per second inside of the ATLAS detector[3] [18]. On tape, each event will consist of roughly 1.3 megabytes of data. Out of sheer necessity due to countless hardware and software limitations (limited storage capacity being a primary concern) the ATLAS trigger system acts to selectively record events in a way that will optimize the possibility of finding new physics within the selection, as well as testing the well established Standard Model.

ATLAS's trigger is implemented in a hierarchy: the most prevalent trigger is the **Level 1 (L1) trigger**, which consists of a hardware system built directly into the detector. Using information collected directly from the calorimeters and muon system, the L1 trigger is activated for events containing high p_t muons, electrons, photons, jets and taus; as well as high E_t and $\not{E}_t$[4]. When activated, the trigger decides within 2.5μs whether the event is to be kept or thrown away. Due to the nominal bunch spacing of 25ns in the LHC, a decision which takes 2.5μs is still far too long in order to keep ahead of the data influx. As a result, the ATLAS trigger employs a buffer to act as a temporary storage space for the selected events, and processes continuously from this stack while data collection is taking place. Ultimately, these selection criteria reduce the event rate from 40 MHz to roughly 75 kHz, and pass the surviving events on to further layers of trigger hierarchy.

The ATLAS **level 2 (L2) trigger** and **High Level Trigger (HLT)** differ from the L1 trigger in that they are both software-based. The L2 trigger processes events online using programmed filters, and further reduces the data rate to roughly 3.5

[3]This is enough data to create a stack of CD-ROMs to the moon and back, twice per year [30]!

[4]The $\not{E}_t$, or **missing transverse energy**, is the negative vector sum of transverse momentum in all cells. This variable is introduced as it may indicate the presence of neutrinos or other neutral or weakly interacting particles. The reconstruction of the $\not{E}_t$ is discussed further in section 3.1.3.

kHz. The event filter is a much more involved process which can take several seconds per event to process, after which the event rate is reduced to a manageable final 200Hz [31]. It is the final step taken online at CERN before the data is distributed to ATLAS tier0 computing centre and then off to the tier1 centres across the grid.

Chapter 3

Event Reconstruction and Selection

3.1 Object Reconstruction

ATLAS events that pass the initial trigger selection are passed along to the tier0 computing centre, which reconstructs events before they are passed along to the tier1 centres. For a refined reconstruction, each object in an event is reconstructed using algorithms specialized for the task. Presented below is an overview of the algorithms used in reconstructing electron, muon, $\not\!\!E_T$ and jets [22].

3.1.1 Electron Reconstruction

Electron identification at the LHC is a key component of many of the searches for new physics underway. ATLAS reconstructs electrons by applying a pair of algorithms:

The first method; **calorimeter-seeded reconstruction**, begins by finding isolated energy deposits (or clusters) in the electromagnetic calorimeter, and then works backward to connect it to track information gathered by the pixel and strip detectors. A cut on the the ratio of energy of the calorimeter cluster to the momentum of the reconstructed track is required to be less than 10 in order to consider the electron candidate. A deficiency between expected electrons and reconstructed electrons may arise when applying this method, as some calorimeter clusters are obscured by material in the detector itself.

The second; **tracker-seeded reconstruction**, instead matches reconstructed pixel and strip detector tracks to clusters in the calorimeter. This method is better suited for finding low-p_T electrons which may not leave large calorimeter deposits.

3.1.2 Muon Reconstruction

ATLAS classifies muons into three different categories during reconstruction, with corresponding algorithms applied to each:

Standalone Muons are those which are reconstructed by finding a set of tracks in the ATLAS muon system and extending it back to the interaction point. The algorithm must make adjustments to the reconstruction due to energy loss in the calorimeter, which is based on which materials the interpolated path crosses. Muons that are classified as 'standalone' but whose interpolated trajectory does not coincide with the primary interaction point are most likely muons produced in the calorimeter due to showers from π and κ particles, and are known as "fake" muons, a background to most processes.

Combined Muons are standalone muons that match to a set of tracks found in the inner detector by the pixel and strip tracking systems. The two sets of tracks are matched using a chi-squared algorithm to determine the quality of the pairing, again accounting for the energy lost in traversing the calorimetry systems and for the magnetic fields in the inner detector and muon systems.

Tagged Muons could be considered the opposite of standalone muons. A tagged muon is reconstructed by finding a set of tracks in the inner detector, then extrapolating the track to the muon system and searching for hits close to the predicted cell. This reconstruction approach also emplys a chi-squared algorithm to rank the nearby hits in order of likelihood.

3.1.3 Missing Transverse Energy Reconstruction

Due to the presence of neutrinos in the dilepton $t\bar{t}$ final state, the missing transverse energy is one of the most important observables to carefully measure and understand. ATLAS employs a pair of algorithms for this task: the **cell-based algorithm**, which weights activated calorimeter cells depending on their energy density; and the **object-based algorithm**, which works with other already-reconstructed objects in the event (electrons, photons, muons, taus and jets) and sums their respective calibrated transverse energies, as found using their own proper reconstruction algorithms.

Cell-Based $\not{E}_T$ Reconstruction

The Cell-Based Reconstruction Algorithm considers $\not{E}_T$ contributions originating from the calorimeter, muon systems and cryostats. The calorimeter term is determined by finding the negative sum of each energy deposit in activated calorimeter cell clusters:

$$\not{E}_T{}^{Calo} = -\sum_{Clusters} E_T$$

where the energy deposits in each cell is scaled depending on the shape of the deposit (EM showers, which tend to have a higher energy density vs. hadronic showers, which tend to have a lower). The muon system term is defined the negative sum of the muon momentum:

$$\not{E}_T^{Muons} = -\sum_{Muons} E_T.$$

If the muon tracks are within $\eta < 2.5$, the muon must be a 'combined muon' reconstructed from corresponding tracks in the inner detector and the muon chambers. For $2.5 < \eta < 2.7$, only tracks in the muon chambers are required ('standalone' muons) [22]. The cryostat term compensates for energy lost in the cryo layer between the EM and hadronic calorimeters. This term may be expressed as:

$$\not{E}_T^{Cryo} = -\sum_{Jets} w\sqrt{E_{EM}^{Last} \cdot E_{Hadronic}^{First}}$$

where w is a weighting factor determined by the shape of the energy deposit (a narrow EM shower vs. a wider Hadronic shower), and the energy terms represent the energy in the last layer of the EM calorimeter and the first layer of the hadronic calorimeter, respectively.

The total missing transverse energy may then be determined as:

$$\not{E}_T = \not{E}_T^{Calo} + \not{E}_T^{Muons} + \not{E}_T^{Cryo} \tag{3.1}$$

3.1.4 Jet Reconstruction

Quarks and gluons created in the collision quickly hadronize to form colour-neutral bound states of 2 (mesons) or 3 (hadrons) individual quarks due to quark confinement. These particles tend to have short lifespans and decay after travelling only a small distance in the detector. The daughter particles produced then re-hadronize and repeat the process. As a result, large showers of particles originate and are detected as energy deposits in the ATLAS hadronic calorimeters, forming the objects referred to as **jets**.

Jet reconstruction poses a set of problems to overcome: unlike electrons and photons, jets are defined entirely by the methodology used in event analysis during the reconstruction process. The theoretical ideal jet reconstruction algorithm would possess the following characteristics [32]:

- **Fully Specified:** The algorithm would precisely make a mapping from the particle list to the jet list.
- **Theoretically Well-Behaved:** The algorithm should not suffer from (or be sensitive to) infrared and collinear instabilities.
- **Independence of Detector:** The algorithm should function to the same level of precision, regardless of cell type, the number of cells, or the size of each cell.
- **Independence of Order:** The algorithm should function equivalently, regardless of the analysis scope (parton-, particle- or detector-level).

Presented below are a pair of jet reconstruction algorithms: the intuitive cone-fitting algorithm mainly used at the Tevatron, and the K_T algorithm currently applied in ATLAS collaboration analysis.

Iterative Cone-Fitting Algorithms

Iterative fixed-cone jet reconstruction algorithms are the most intuitive method for building jets out of event data. Using these methods, all calorimeter cells are first ranked in order of p_T. Next, all cells lying within cones of predetermined radius $R_{cone} > \sqrt{\Delta\eta^2 + \Delta\phi^2}$ are selected and grouped as a prototype jet. The combined four-momentum of these objects is then computed, and this direction forms the major axis of the next iteration's cone. This process is repeated until the shift in direction of the jet falls below a predetermined threshold, when the prototype is defined as a stable jet.

There are numerous theoretical problems associated with this method of jet reconstruction: in particular, this algorithm is not **infrared safe** [33]. This concept is illustrated in figure 3.1: the cone-fitting algorithm is highly susceptible to soft radiation. For example, if two partons exist at a distance from each other, the standard algorithm will reconstruct these particles as a pair of jets. If, however, there exists a soft gluon between the partons, the algorithm is likely to instead identify the entire group as one single jet: the presence of this low-energy radiation radically alters the outcome of the analysis, an effect which is extremely unphysical and hence, undesirable.

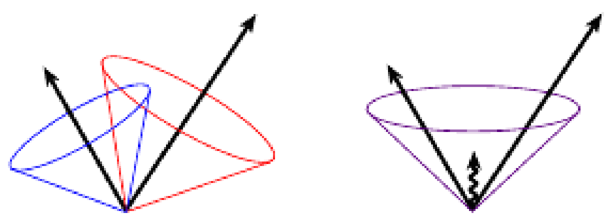

Figure 3.1: An illustration of an infrared-type sensitivity: a soft gluon is radiated between a pair of partons, causing a different interpretation of the event by the cone-fitting algorithm [33].

K_T Recombination Algorithm

In order to bypass the limitations of the cone-fitting algorithm, the default ATLAS jet reconstruction algorithm is instead based on the K_T method of reconstruction. The K_T method is a process in six steps [33]:

1. Using output from the calorimeter cells, **preclusters** are formed and each assigned a massless four-vector:

$$(E, \vec{p}) = E(1, \cos\phi \sin\theta, \sin\phi \sin\theta, \cos\theta). \tag{3.2}$$

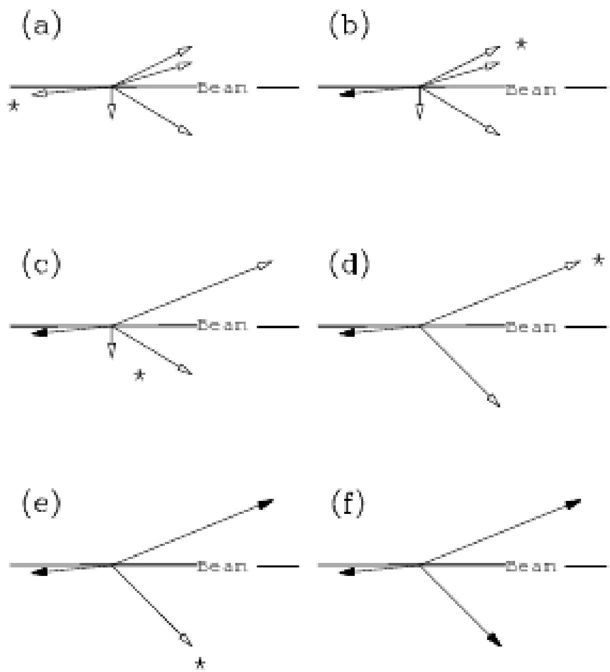

Figure 3.2: An illustration of the K_T jet reconstruction algorithm. Each successive image demonstrates a step in the K_T process - either merging a pair of objects, or selecting a pair to compare [33].

For each four-vector, the transverse momentum and rapidity are then defined:

$$p_T^2 = p_x^2 + p_y^2 \tag{3.3}$$

$$y = \frac{1}{2} \ln \left(\frac{E + p_x}{E + p_y} \right). \tag{3.4}$$

2. For each precluster i, define

$$d_i = p_t^2. \tag{3.5}$$

For each *pair* of preclusters (i, j) such that $i \neq j$, define

$$\begin{aligned} d_{i,j} &= min(p_{Ti}^2, p_{Tj}^2) \left(\frac{\Delta R_{i,j}^2}{D^2} \right) \\ &= min(p_{Ti}^2, p_{Tj}^2) \left(\frac{(y_i - y_j)^2 + (\phi_i - \phi_j)^2}{D^2} \right) \end{aligned} \tag{3.6}$$

where D is a distance parameter defined by the user.

3. The set $\{d_i \cup d_{i,j}\}$ is minimized. This minimum element is defined to be d_{min}.

4. Should d_{min} belong to the set of $\{d_{i,j}\}$'s, then the ith and jth elements are removed from the set and replaced with a new precluster $(E_k, \vec{p}_k)$ such that

$$E_k = E_i + E_j \tag{3.7}$$

$$\vec{p}_k = \vec{p}_i + \vec{p}_j. \tag{3.8}$$

5. Should d_{min} belong to the set of $\{d_i\}$'s, then the ith element is not mergeable. This element should be removed from the set - it is defined to be a jet.

6. This process should be repeated from step 1, until the set of preclusters $\{d_i \cup d_{i,j}\}$ is empty.

The K_T reconstruction algorithm is much more reliable than the cone-fitting method, as the process is infrared safe. In typical atlas analysis, $D = 0.4$ or $D = 0.6$ are used, depending on whether narrow or wide jets are desired [22]. One further difference between the analysis used in typical ATLAS analysis (called the "anti-K_T" algorithm) from the standard K_T algorithm presented in this section: in the anti-K_T algorithm, the jet of higher energy is added to that of lower energy in the case of jet overlap.

3.2 Event Selection

To identify $t\bar{t}$ events, the ATLAS top working group has outlined a set of event selection cuts based on the kinematics of $t\bar{t}$ interactions in the dilepton channels:

1. To select the leptonic decay of the W's; require 2 isolated leptons (ee, $\mu\mu$ or $e\mu$) with $P_t > 20$ GeV.

2. Veto events when the combined invariant mass of leading leptons falls close to the Z peak, in order to suppress dominant Drell-Yan backgrounds ($|Mass(ee) - 91| < 5$ or $|Mass(\mu\mu) - 91| < 10$).

3. To select the b-jets produced by the t decay; require at least 2 jets with $P_t > 20$ GeV.

4. Require large missing transverse energy ($\not{E}_t > 40$ GeV ee or $\not{E}_t > 30$ GeV $\mu\mu$) or large H_t ($H_t > 150$ GeV $e\mu$)[1].

3.2.1 Monte-Carlo Challenge Validation

In order to validate the performance of the analysis code under development, the ATLAS Top Cross-Section Working Group has produced a $t\bar{t}$ Monte-Carlo sample, and provides a standard set of event selection cuts to be applied as follows:

[1] H_t is defined as the sum energy of all selected objects (jets, leptons) in the transverse plane.

1. True dilepton events: the event contains at least two leptons which match to the generator-level output.

2. $>=$ 2 selected leptons with $p_t > 20$GeV

3. Jet Cleaning: reject all selected events with 'bad'[2] jets or with no jets possessing $p_t > 10$ GeV.

4. Non-collision background rejection: require a vertex with $N_{tracks} > 4$.

5. Z Window: for the leading pair of leptons, require:

   - $|$ Mass$(ee) - 91| > 5$ GeV (Dielectron channel)
   - $|$ Mass$(\mu\mu) - 91| > 10$ GeV (Dimuon channel)

6. $\not{E}_t/H_t$ Requirements:

   - $\not{E}_t > 40$ GeV (Dielectron channel)
   - $\not{E}_t > 30$ GeV (Dimuon channel)
   - $H_t > 150$ GeV (Mixed channel)

7. $>=$ 2 Jets with $p_t > 20$GeV and $\eta > 2.5$

8. 2 and only 2 Leptons.

9. Leptons have opposite sign.

10. e / μ overlap removal - reject the event if any electron has the same inner detector track as any muon.

11. Trigger Select - ELECTRON (*) trigger for ee channel. Trigger matching for muons is not yet implemented, therefore this cut has no impact on $\mu\mu$ and $e\mu$ events.

[2] i.e. not meeting the conditions defined in section 3.2.2.

12. Trigger Matching: at least one lepton in the event must match the trigger (*ee* channel only).

13. Both leptons match to truth at generator level.

By ensuring that each group or institution attempting to perform a cross-section measurement obtains the same values at each step in the analysis cutflow, the Working Group is assured that all analysis codes are performing appropriately. The event selection code being developed for this project was validated successfully using the MC Challenge method, yielding similar results to those obtained by the top group at TRIUMF.

3.2.2 Jet Quality Cuts

After preliminary event-selection has occurred, it is crucial to ensure that all remaining events have jets which are well-behaved. Due to the complex nature of jet objects and the nature of their particular reconstruction process (as outlined in sec. 3.1.4), there are several considerations which must be made [34][35]:

- Hardware failures in certain HEC cells occasionally cause noise bursts, which manifest themselves as large-energy events in extremely localized areas (on the order of 10-15 GeV in one or two cells), regardless of whether or not collisions are occurring in ATLAS. To remove these events, it is required that no jet may deposit over 90% of its energy in fewer than 5 unique calorimeter cells ($n_{90} < 5$), while at the same time the fraction of energy deposited in the calorimeter by the jet (f_{HEC}) is greater than 80% of the total event energy.

- In order to eliminate bad-quality jets in the electromagnetic calorimeter, it is required that no jet with greater than 95% of its energy in the EM calorimeter ($f_{EM} > 95$) possess a fitting quality factor[3] of more than 0.8 ($f_Q > 0.8$).

[3]The fitting quality factor is a measure of the difference between the readout pulse from the electromagnetic calorimeter, and the reference curve used in reconstruction software.

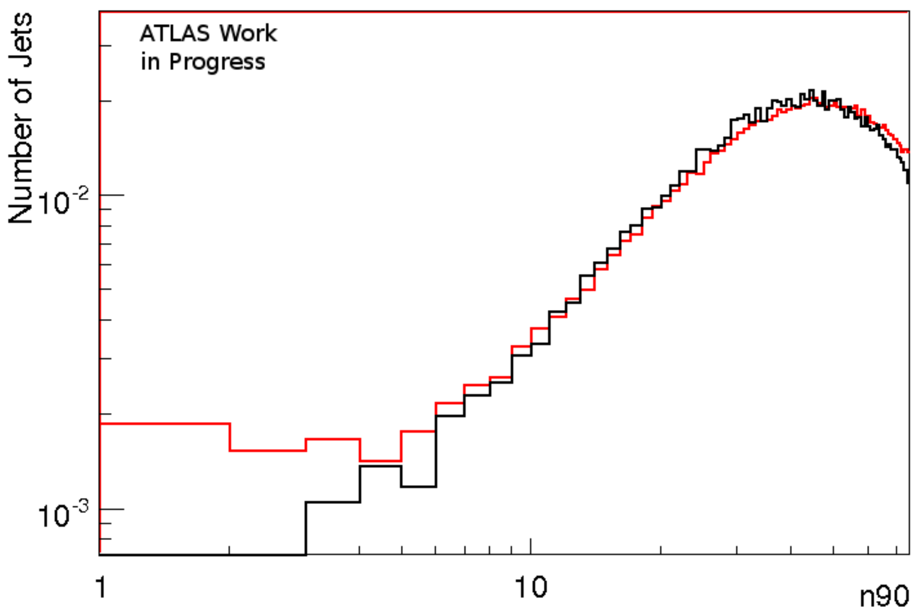

(a) n_{90}

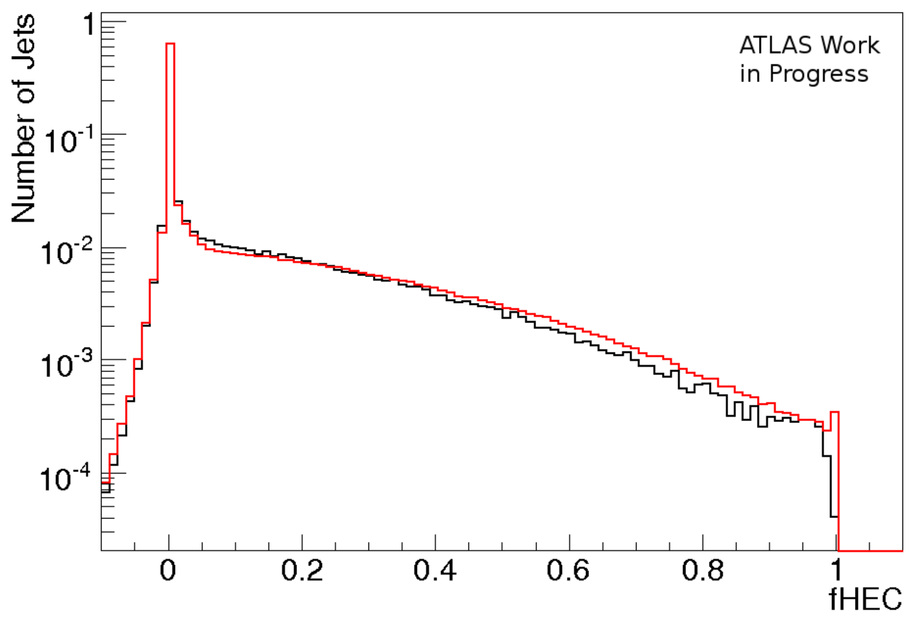

(b) f_{HEC}

Figure 3.3: Histograms of n_{90} and f_{HEC} before jet cleaning cuts are applied, with overlaid Monte Carlo prediction [**BLACK**] and early run data [**RED**] (area-normalized in order to allow comparison).

- In order to remove events with jets resulting from collisions of beam particles which arrive either before or after the bunch ("beam halo" events), as well as events with jets from photons due to cosmic ray muon decay, an event timing cut requires that the time-window in which a jet occurs fall within 50ns of the bunch crossing associated with the event.

3.3 Standard Model Backgrounds

3.3.1 Diboson (WW, ZZ, WZ)

Diboson processes, in which a WW, ZZ or WZ pair are produced, may mimic $t\bar{t}$ events. In WW production, both W's may decay as W's produced by a true $t\bar{t}$ event, reproducing all final-state particles except for the b-jets. ZZ events may masquerade as signal events if electrons are produced and mis-identified as jets, in association with properly tagged electrons or muons and $\not{E}_T$ obtained during reconstruction due to mismeasurement (as in the Drell-Yann background, discussed in section 3.3.3). In a WZ event, a combination of the above scenarios may occur: should the W decay into a lepton and neutrino, and the Z into a pair of electrons which are then potentially mis-tagged as jets, all signal elements may again be present.

Single top events represent a similar background: in figure 1.3 it is shown that two possible channels of single-top production have a final state containing a W and a t (channels d and e). As the t will decay as $t \to Wb$, the final state will then contain a pair of W's and at least one b-jet, with another jet potentially entering from a mis-identified electron.

Table 3.1: Summary of standard model background information for a sample normalized to 32.1 pb^{-1}, for a standard event selection with the z-veto and $\not\!\!E_T$ cuts removed. The Drell-Yan process contributes on the order of 10-100 times more events than any other background. The $t\bar{t}$ sample (the signal) is listed for comparison.

Sample		Cross-Section	Number of Events ($\mathcal{L}$=32.1 pb^{-1})
$t\bar{t}$	T1_McAtNlo	88.2211	29.8072
Single Top	Wt_McAtNlo	14.581	1.48
$Z \rightarrow \mu\mu$	ZmumuNp0	802.394	124.2
	ZmumuNp1	162.016	167.176
	ZmumuNp2	48.312	392.664
	ZmumuNp3	13.542	150.409
	ZmumuNp4	3.416	39.9405
	ZmumuNp5	0.976	11.5524
$Z \rightarrow \tau\tau$	ZtautauNp0	802.028	0.0849788
	ZtautauNp1	162.26	0.496202
	ZtautauNp2	49.288	1.58273
	ZtautauNp3	13.42	0.313467
	ZtautauNp4	3.538	0.454582
	ZtautauNp5	0.854	0.16481
Diboson ZZ	ZZinclNp0	0.59774	1.38959
	ZZinclNp1	0.27225	0.875864
	ZZinclNp2	0.10648	0.490145
	ZZinclNp3	0.003388	0.0165004
Diboson WW	WWinclNp0	2.47929	0.0542895
	WWinclNp1	1.19427	0.216259
	WWinclNp2	0.53361	0.640791
	WWinclNp3	0.21538	0.338181
Diboson WZ	WZinclNp0	0.80344	1.37042
	WZinclNp1	0.48279	1.66045
	WZinclNp2	0.26741	1.06718
	WZinclNp3	0.11253	0.480713

3.3.2 W+Jets

The production of W bosons along with additional hadronic jets represents the major background to $t\bar{t}$ production in the single-lepton channel, though it poses a smaller contribution in the dilepton case. Events of the form $W \to \ell\nu$ produced in conjunction with gluons radiated by the incident particles contain elements which closely mimic a $t\bar{t}$ event final state: an outgoing lepton, at least two hadronic jets and missing transverse energy due to the neutrino [36]. Should one of the produced jets be mis-tagged as an electron, the event could pass for a signal event in the dilepton channel.

Single top events with a t and one or two other quarks in the final state (channels a, b and c in figure 1.3) mimic $W + Jets$ events, as they will contain a W and b-jet from the top, along with additional jets from the other final-state hadrons. This in turn makes them a background to the $t\bar{t}$ interaction.

3.3.3 Drell-Yan Process ($Z \to \ell\bar{\ell}$)

The Drell-Yan process occurs when a quark of one incident proton annihilates with an antiquark of the other during a collision, producing a virtual Z-boson which then decays into a lepton-antilepton final state[4]. It represents the primary background to the $t\bar{t}$ interaction, and as such requires careful consideration and study in order to minimize its footprint in the analysis in as efficient and precise a manner as is possible. When one (or both) of the incident quarks radiate gluons before annihilating, the final state will have both high-energy jets and a pair of high-energy, oppositely charged leptons: closely matching the selection criteria for $t\bar{t}$ events laid out in section 3.2. Furthermore, due to the finite nature of the ATLAS detector's resolution and the limited capacity of $\not{E}_T$ reconstruction

[4]The process was initially theorized by Sidney Drell and Tung-Mow Yan in 1970 [37] and first observed in Brookhaven's Alternating Gradient Synchrotron by Christiensen *et al.* [38].

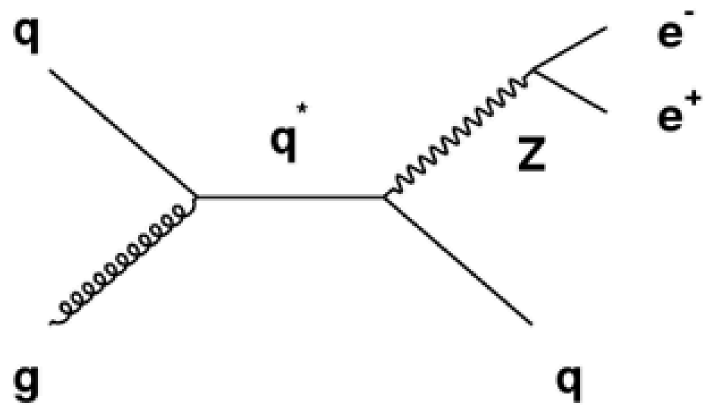

Figure 3.4: A feynman diagram of the Drell-Yan production process, which proceedes as $q\bar{q} \rightarrow \ell\bar{\ell}$ and is mediated by a virtual Z-boson.

algorithms, it is possible for an event to be reconstructed in software with a non-zero value of missing transverse energy. The Drell-Yan $\not{E}_T$ distribution is shown in figure 3.5a, where it is apparent that in most cases this artificial value is quite small, though on occasion it can approach a level comparable to that of a true $t\bar{t}$ event. This sharply-falling distribution differs quite largely from that characteristic of $t\bar{t}$ events, which tends to have a peak at some nonzero value of $\not{E}_t$ due to the presence of high-energy neutrinos produced by the decay of the W bosons. It is in-part due to the presence of the sharply-falling Drell-Yan distribution that there is a threshold cut on $\not{E}_t$ in standard analysis.

Another major difference present in the kinematics of the Drell-Yan process which distinguishes it from the $t\bar{t}$ interaction is the presence of an on-shell Z-boson, which produces a peak in the invariant mass of the event's leading lepton pair at 91.18 GeV/c^2, corresponding to the PDG Z boson mass [10] (which would be observed near 90 GeV/c^2 in figure 3.7a). Because the leptons in $t\bar{t}$ events are produced by W's, the distribution of mass is isotropic. This difference results in discarding all events falling within the 'Z-window' of the analysis, whose width differs depending on the channel (see section 3.2 for detailed values).

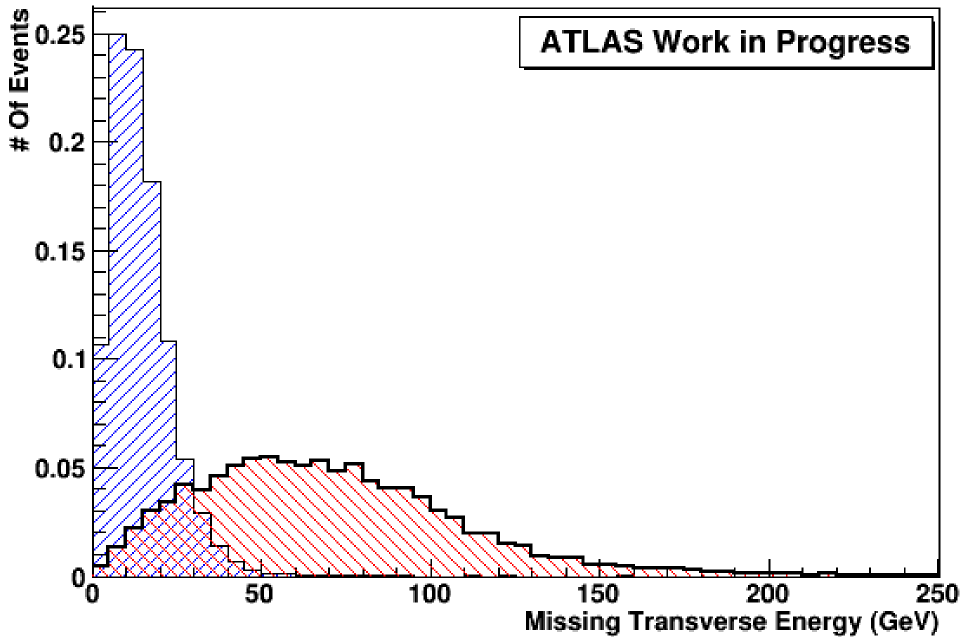

(a) Missing Transverse Energy

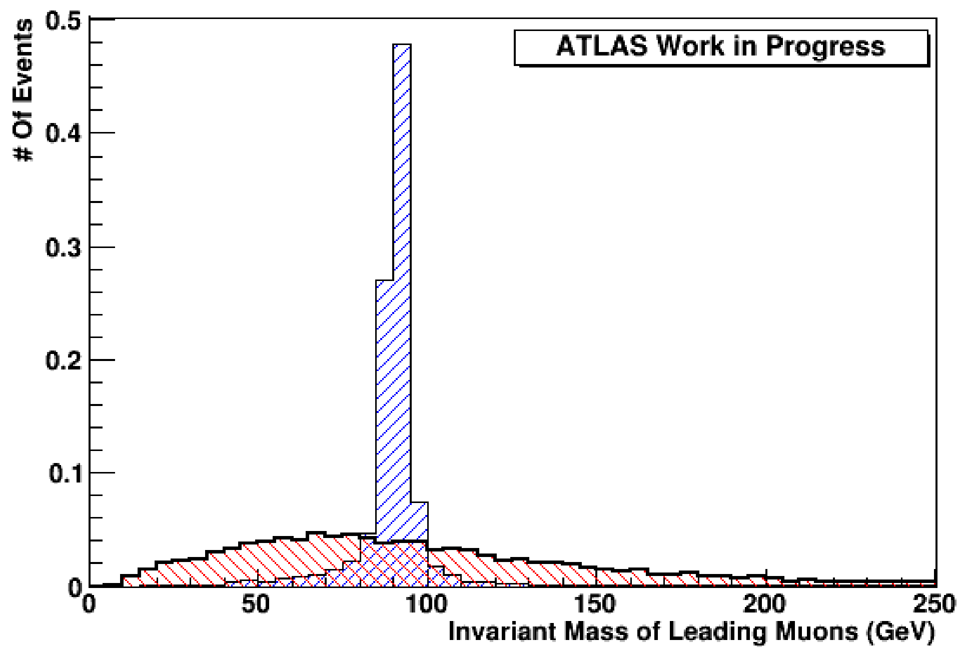

(b) Invariant Leading Lepton Mass

Figure 3.5: A comparison of kinematic distributions of discriminating variables for Drell-Yan **[BLUE]** and ttbar **[RED]** events (area-normalized in order to allow geometric comparison).

3.3.4 QCD Multijet Production

QCD mutijet production forms a background to the $t\bar{t}$ process when jets are misidentified as leptons and missing transverse energy is obtained due to the mis-measurement of object energy in the ATLAS calorimetry systems (though real missing energy could also be produced in association with b and c quarks). This background was measured to be consistent with zero in the Top-WG analysis [12], and so is also assumed to contribute zero events in this analysis.

3.4 Drell-Yan Background Estimates

In order to measure how many background Drell-Yan events are expected with our signal events during the analysis, the ATLAS Top-WG used a data-driven approach to obtain an estimate. As shown in figure 3.6, the event missing transverse energy was plotted against the invariant mass of the leading lepton pair for both data and Monte Carlo samples. This plot was subsequently divided into nine subzones, $A \rightarrow I$ $(1 \rightarrow 9)$ according to the nine regions defined by the $\not{E}_T$ and invariant mass (illustrated in figure 3.6). By assuming that the two variables are uncorrelated, it is possible to establish an estimate for the number of Drell-Yan events in the $t\bar{t}$ signal region using the similarity relationships laid out by Cranmer *et al* [39]:

$$A_{Est} = G_{Data}\left(\frac{A_{MC}}{G_{MC}}\right)\left(\frac{B_{Data}}{H_{Data}}\right)\left(\frac{H_{MC}}{B_{MC}}\right) \tag{3.9}$$

$$C_{Est} = I_{Data}\left(\frac{C_{MC}}{I_{MC}}\right)\left(\frac{B_{Data}}{H_{Data}}\right)\left(\frac{H_{MC}}{B_{MC}}\right). \tag{3.10}$$

which in turn yields a value of the statistical uncertainty on $\sigma_{t\bar{t}}$. In the analysis presented below (see ch.5) the statistical uncertainty is dominated by that on the data, as the MC samples have large statistics. A different method was therefore used to estimate the statistical uncertainty, outlined in section 5.3.

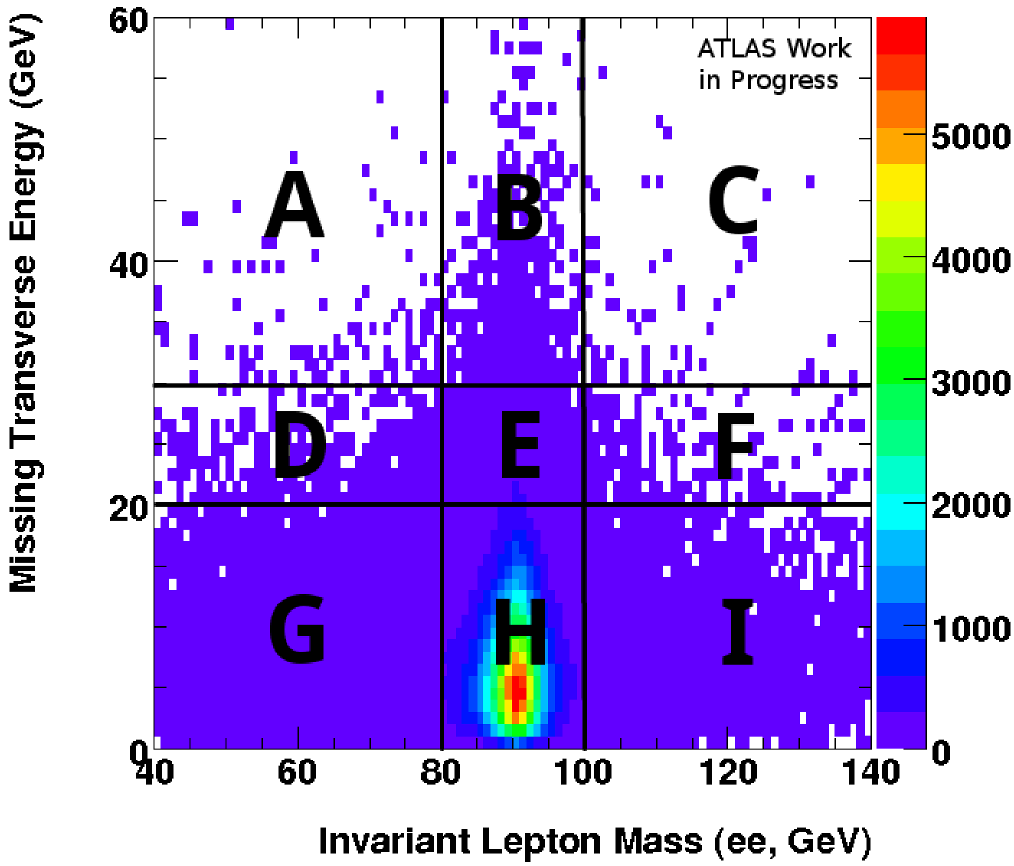

Figure 3.6: Event $\not{E}_t$ vs. leading lepton invariant mass, plotted from $\mu\mu$ MC samples for use in estimating contributions from Drell-Yan backgrounds in signal zones (annotated). Note the Z peak near 90GeV/c^2.

3.5 Kinematic Distributions

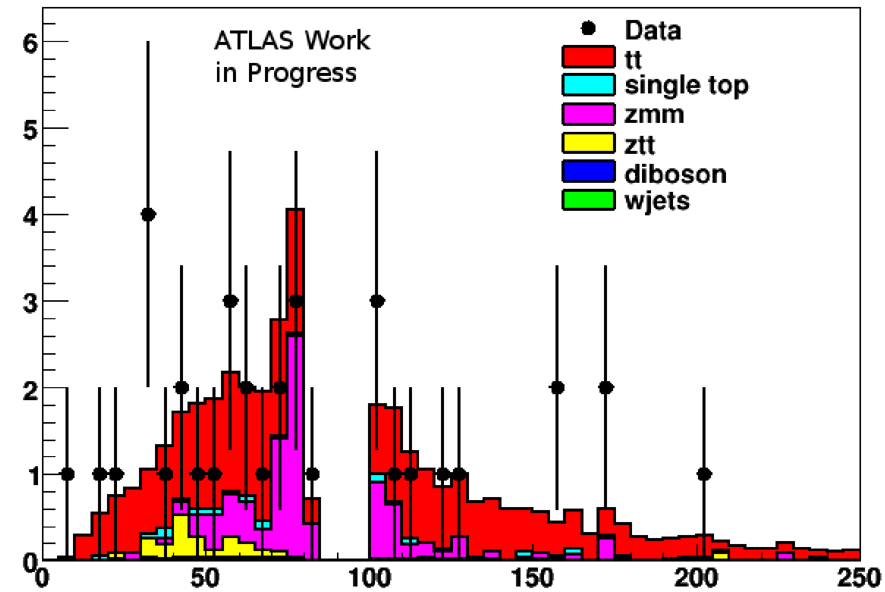

(a) Leading Muon Invariant Mass.

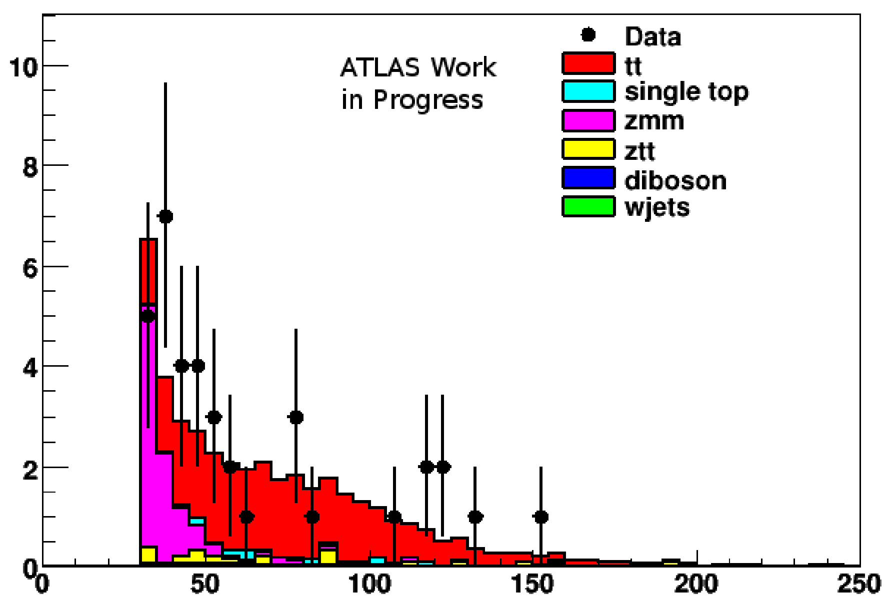

(b) Missing Transverse Energy

Figure 3.7: Kinematic distributions for the 2010-7 TeV data, as well as Monte-Carlo samples for $t\bar{t}$ and relevant backgrounds after MC-challenge cuts have been applied.

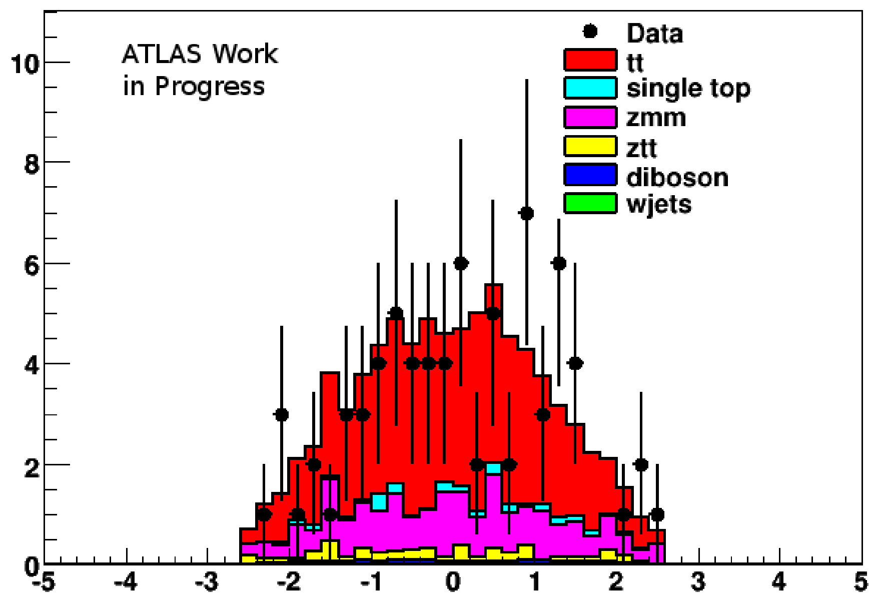

(c) Leading Muon η

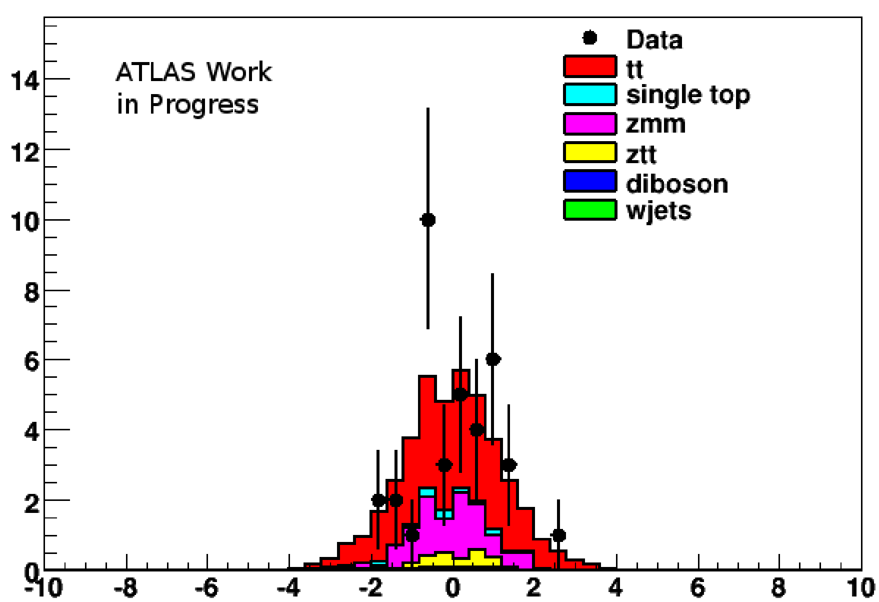

(d) Leading Muon $\Delta\eta$

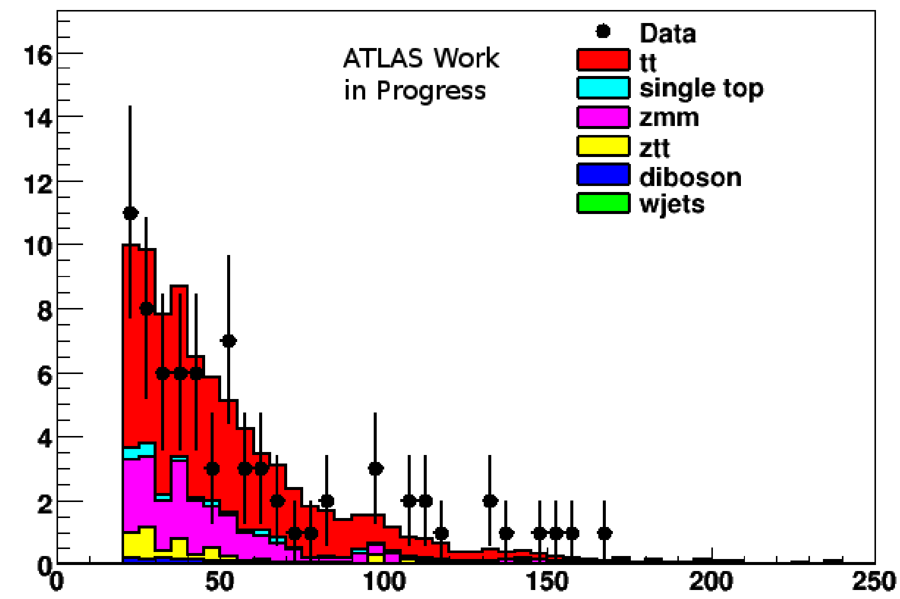

(e) Leading Muon p_T

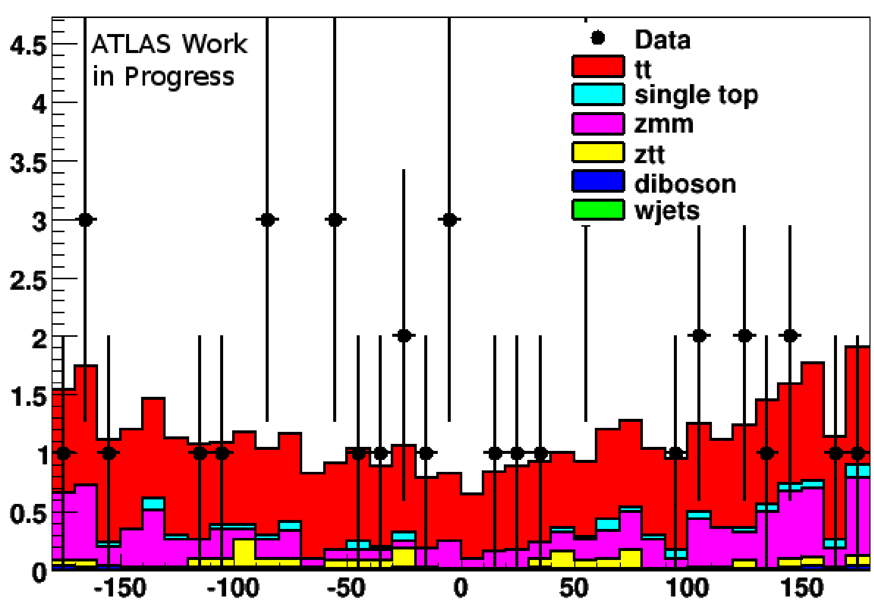

(f) Leading Muon $\Delta\phi$

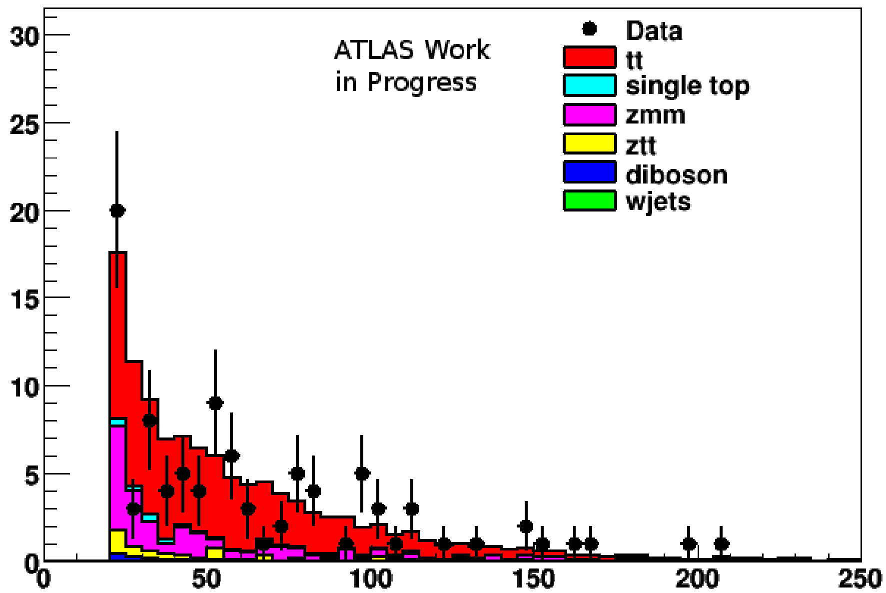

(g) Leading Jet p_T

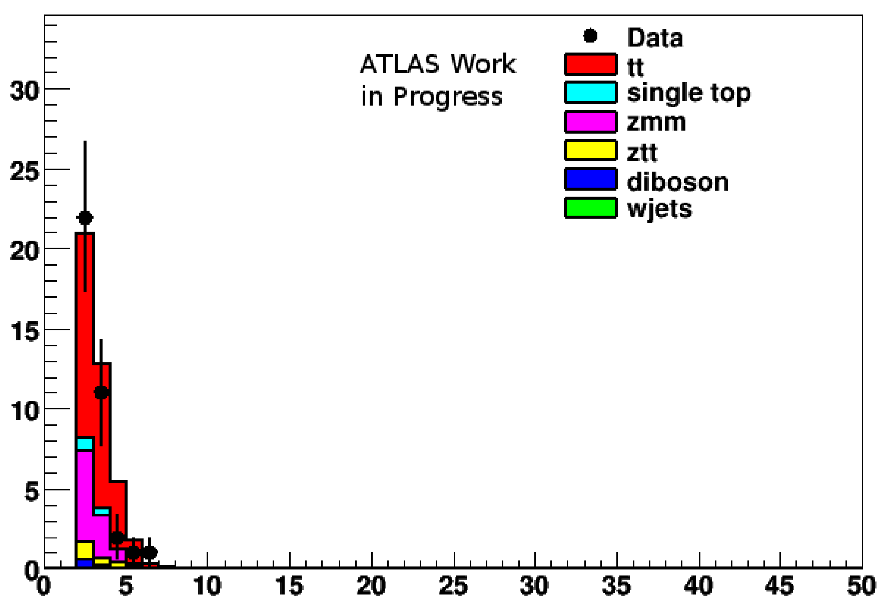

(h) Number of Jets

Chapter 4

Strategy for Cross Section Measurement

4.1 ATLAS Top-WG Results

A preliminary measurement of the $t\bar{t}$ cross section was published by ATLAS's top working-group with a dataset of 35.3 pb^{-1} [12], using a 'cut and count' approach. By applying an event selection similar to that outlined in section 3.2 in order to suppress the relevant backgrounds and by using data-driven methods similar to those outlined in section 3.4 to estimate the number of background events in signal zones, the working group published a cross-section measurement of

$$\sigma_{t\bar{t}} = 194^{+57}_{-51}\,^{+32}_{-20}\text{ pb}$$

in the di-muon channel (where the first listed uncertainty is statistical and the second is systematic). Because of the nature of this analysis method, each cut made reduced the total acceptance of the analysis (ε in equation 1.2), contributing among other factors to the statistical uncertainties in the measurement.

4.2 RooFit and Likelihood Fitting

As shown in eqn. 1.3, the cross-section uncertainty is inversely proportional to the number of signal events, revealing one possible area in which the uncertainty may be reduced by harnessing an alternative analysis method. One approach to increasing the acceptance is to loosen the event selection criteria, preserving signal events but also allowing more background events to pass selection. In order to distinguish between the signal and background events after preliminary event selection has taken place, a binned likelihood fit was constructed.

RooFit, a toolkit developed by the BaBar collaboration for the ROOT analysis software, was utilized for this analysis. RooFit adds functions for modelling statistical distributions of physical processes to ROOT's library of functions for graphically manipulating data in an object-oriented manner. By using RooFit, different distributions may be constructed from ROOT Histogram objects, and easily manipulated using predefined operations such as addition and convolution, among others. RooFit is also capable of generating 'toy' Monte Carlo datasets from a distribution: sets of points created using Poisson statistics which possess the same statistical properties as a set of measured data ideally would if they were described by a statistical distribution. RooFit may then perform fitting tasks on the dataset - either a toy one, or a preset histogram such as one describing a kinematic variable of the LHC dataset.

Binned likelihood fitting [40] operates by comparing a theoretical model to a particular set of data $\{x_1, x_2, ..., x_N\}$, and attempts to maximize the Poisson probability that the data in each bin corresponds to the model by varying a free parameter - in this case, the number of events (or, the integral of the histogram). The likelihood is defined by the product of each bin's individual probabilities:

$$L(x_1, x_2, ..., x_N; a) = \prod_i P(x_i; a) \tag{4.1}$$

Consider the example outlined in figure 4.1. A given physical process under consideration is associated with a simple predicted signal distribution (fig. 4.1a) and a predicted background distribution (fig. 4.1b). Using RooFit, pairs may be added together binwise in order to produce a distribution representative of that acquired performing measurements of this process (fig. 4.1c). From this theoretical data distribution, RooFit may produce datasets such as that shown in fig. 4.1d, which may then be fit using a linear combination of the signal and background histograms, leaving the area under each (or, the number of events) as the floating parameter of the fit. In doing so many times, the fit will attempt to extract the most likely number of signal and background events from the dataset. By performing many pseudo-experiments where this toy data is fit with the statistical model, it is possible to create a likelihood distribution which may then be maximized.

Such an analysis would be valuable in the examination of LHC data. Figure 4.2 again illustrates the previous example, but with a signal distribution corresponding to the invariant mass of the leading muons in a $t\bar{t}$ interaction, and a background distribution corresponding to that of the Drell-Yan process (note the characteristic Z-peak near 90 GeV/c^2). By adding these histograms together, we obtain a Monte-Carlo model with which we may validate our fit. After the fit has been validated, we may apply the fitting algorithm to the corresponding invariant mass distribution drawn from the LHC 2010-7 TeV dataset, and in doing so obtain a measurement of N_{sig} and N_{BG} (as in eqn. 1.2) to use in our cross-section measurement.

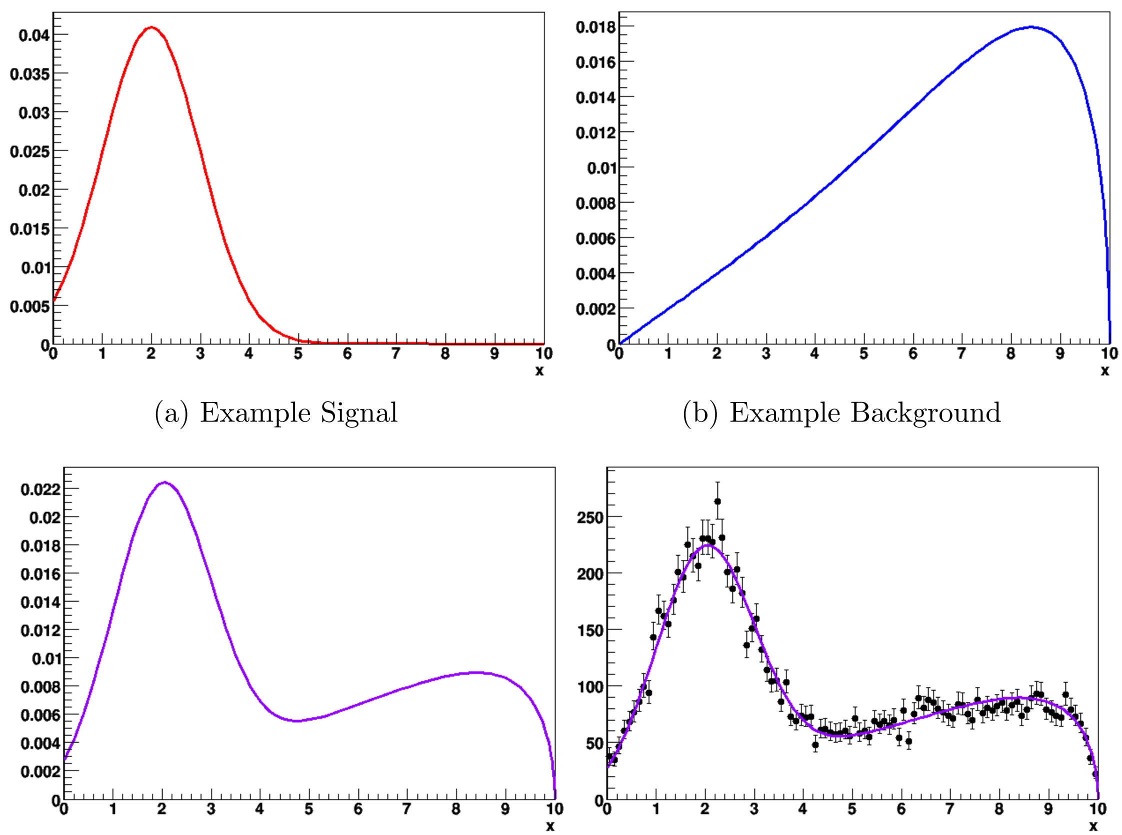

(a) Example Signal

(b) Example Background

(c) Example Data Distribution

(d) Example Generated Dataset

Figure 4.1: A model RooFit experiment.

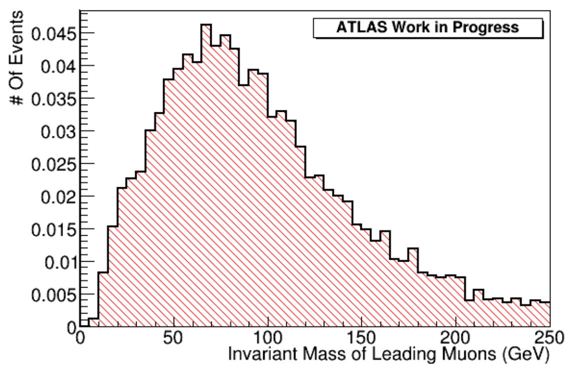

(a) Signal: $t\bar{t}$ (MC)

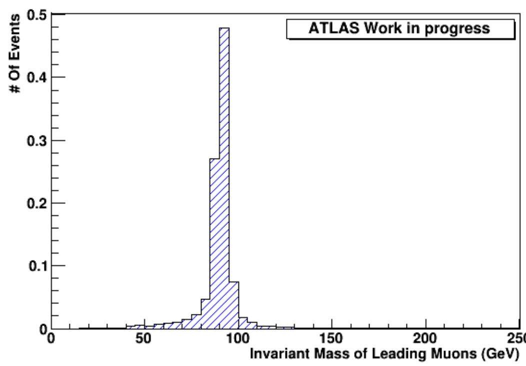

(b) Background: Drell-Yan (MC)

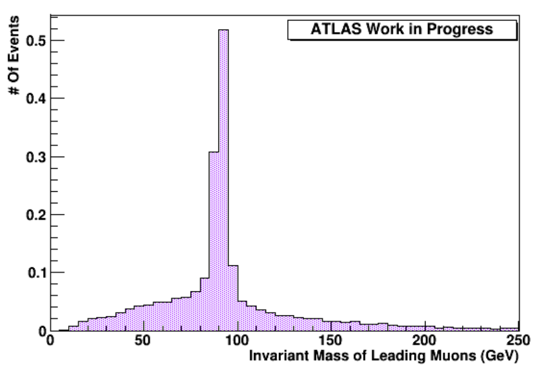

(c) Signal + Background (MC)

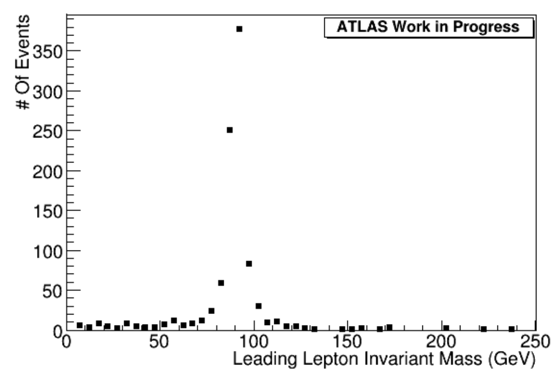

(d) LHC 2010-7 TeV Dataset

Figure 4.2: A collection of the various histograms used in making a measurement using RooFit. In this case, the invariant mass of the event's leading muon pair is used as the discriminating kinematic.

As the likelihood fitting algorithm is developed, it will be simultaneously validated: since the number of true (expected) signal and background events for a given data sample is input, it will be easy to determine whether or not the fit is behaving as it is expected to. This is crucial information to obtain during Monte-Carlo trials, since this knowledge of the 'truth' is hidden when running over LHC data. The focus of the analysis now shifts to an effort to determine the most discriminating kinematic variables: those variables whose signal and background spectra are distinct enough for the fit to be able to distinguish the shape of each curve from their sum. Each variable's relative effectiveness will be evaluated in terms of three *figures of merit*:

- **Mean number of events predicted**, should be equal to true number of events, N_{true}.
- **Statistical Uncertainty**, should ideally be close to $\sqrt{N_{true}}$.
- **Pull**, the difference between the number of events calculated by the fit and the true number, or a measurement of the bias in the cross-section measurement. The pull should ideally be a Gaussian distribution centered at 0 and of width 1.

Chapter 5

Results

5.1 Acceptance

The acceptance (ε in equation 1.2) of a given process is the ratio of the number of these events passing a given event selection to the total number of events that occurred. It takes into account necessary branching ratios and filters applied for an analysis, and may be defined as:

$$\epsilon = \frac{N_{AfterCuts}}{N_{Generated}} = \frac{N_{AfterCuts} \cdot \epsilon_{filter}}{N_{BeforeCuts}} \tag{5.1}$$

where ε_{filter} represents the branching ratios and filter efficiencies of the processes that were included in the sample generation. In this analysis of the $t\bar{t}$ process, events in which both W's decay hadronically were filtered from the generation process:

$$\varepsilon = \frac{N_{AfterCuts} \cdot -(1 - \Gamma_{W \to q\bar{q}, W \to q\bar{q}} \cdot \Gamma_{W \to q\bar{q}, W \to q\bar{q}})}{N_{Generated}}. \tag{5.2}$$

For the purposes of this analysis, we consider only dimuon events (events in which each W decays as $W \to \mu\nu$). Using the appropriate branching ratio, we find:

$$\varepsilon = \frac{5908 \cdot 0.5430}{773167} = 0.004149 \tag{5.3}$$

for the standard event-selection cuts outlined in section 3.2.1, and

$$\varepsilon = \frac{8138 \cdot 0.5430}{773167} = 0.005715 \tag{5.4}$$

for the same cuts with the Z-veto and $\not{E}_t$ cuts removed.

Only the acceptance corresponding to the signal sample (in this case, the $t\bar{t}$ Monte-Carlo sample) must be known. This is due to the fact that for a given luminosity sample $\mathcal{L}$ consisting of

$$N = N_{Signal} + N_{BG}$$

events, the signal will possess a certain cross-section

$$\sigma_{Signal} = \frac{N_{Signal}}{(\mathcal{L} \cdot \varepsilon_{Signal})}.$$

Re-writing the expression for N in terms of this expression for σ_{Signal} gives

$$N = \sigma_{Signal} \cdot \mathcal{L} \cdot \varepsilon_{Signal} + N_{BG}$$

which may be solved for the signal's cross-section:

$$\sigma_{Signal} = \frac{N - N_{BG}}{\mathcal{L} \cdot \varepsilon_{Signal}},$$

an expression involving only the signal sample's acceptance.

5.2 Preliminary Likelihood-Fit Cross-Section Measurements

A likelihood fit as described in section 4.2 was performed to obtain a value of the $t\bar{t}$ cross-section in the dimuon channel. In order to validate the fit, a set of 10 000 pseudo-experiments was performed for various kinematic variables. In these pseudo-experiments, the number of signal and Drell-Yan background events were allowed to float in the fit, while the other backgrounds were normalized to fixed values based on their cross section and the luminosity of the dataset (32.1 pb^{-1}). In the results presented below in table 5.1, the sample contained 30 true signal and 570 true Drell-Yan background events.

Table 5.1: Summary of likelihood fitting algorithm validation for signal and background channel for various kinematic variables.

Kinematic Variable	Pseudo-experiment Results					
	Signal			Drell-Yan		
	N_{sig}	Stat. Err.	Pull σ	N_{bg}	Stat. Err.	Pull σ
Missing E_T	31	8	1.001	560	25	1.014
Invariant Mass	39	13	0.970	565	26	1.023
$\Delta\eta$, Leading Muon Pair	35	10	1.00	560	50	1.055
Leading Muon p_T	50	45	0.814	590	100	1.118
Leading Jet p_T	55	10	0.938	550	50	1.043
Number of Jets	20	20	0.975	580	50	1.061
Leading Muon η	*Fit performance inadequate.*					
$\Delta\phi$, Leading Muon Pair	*Would not converge.*					

As a result of the pseudo-experiments, one kinematic variable was chosen to perform the cross-section measurement: the missing transverse energy (fig. 5.1). Other kinematic variables exhibited poor performance. The missing transverse energy was then used to extract the number of signal and background events from the 2010-7 TeV dataset, again by leaving the number of signal and Drell-Yan background events float in the fit while holding the other backgrounds at fixed values (given in table 3.1). The extracted value for N_{sig} was in turn used to calculate a cross-section value according to equation 1.2, resulting in a measurement of

$$\sigma_{t\bar{t}} = 148.8 \pm 39.8\ (Stat.)\ \text{pb}. \tag{5.5}$$

At this point, the reported uncertainty considers only the statistical uncertainty found on the floating number of signal events in the fit. Consideration of additional statistical uncertainties from the fixed backgrounds will follow in section 5.3, and of systematic uncertainty due to the jet energy scale in section 5.4.1.

5.3 Statistical Uncertainties from Fixed Background Samples

Only the number of signal events and the number of Drell-Yan background events were left as floating parameters in the fit. Contributions due to the other backgrounds (diboson, single top, W+jets and $Z \to \tau\tau$ as outlined in section 3.3) were assigned fixed values by normalizing the corresponding Monte Carlo samples to the luminosity of the data by using the appropriate cross-sections. These additional backgrounds contribute additional statistical uncertainties to the measured cross-section value, according to

$$\Delta N_{Norm} = \frac{\sqrt{N'}\mathcal{L}}{\mathcal{L}_{MC}} \tag{5.6}$$

where N' is the raw number of events passing selection cuts before normalization, N_{Norm} is number of events before and after normalizing the sample, and $\mathcal{L}$ and

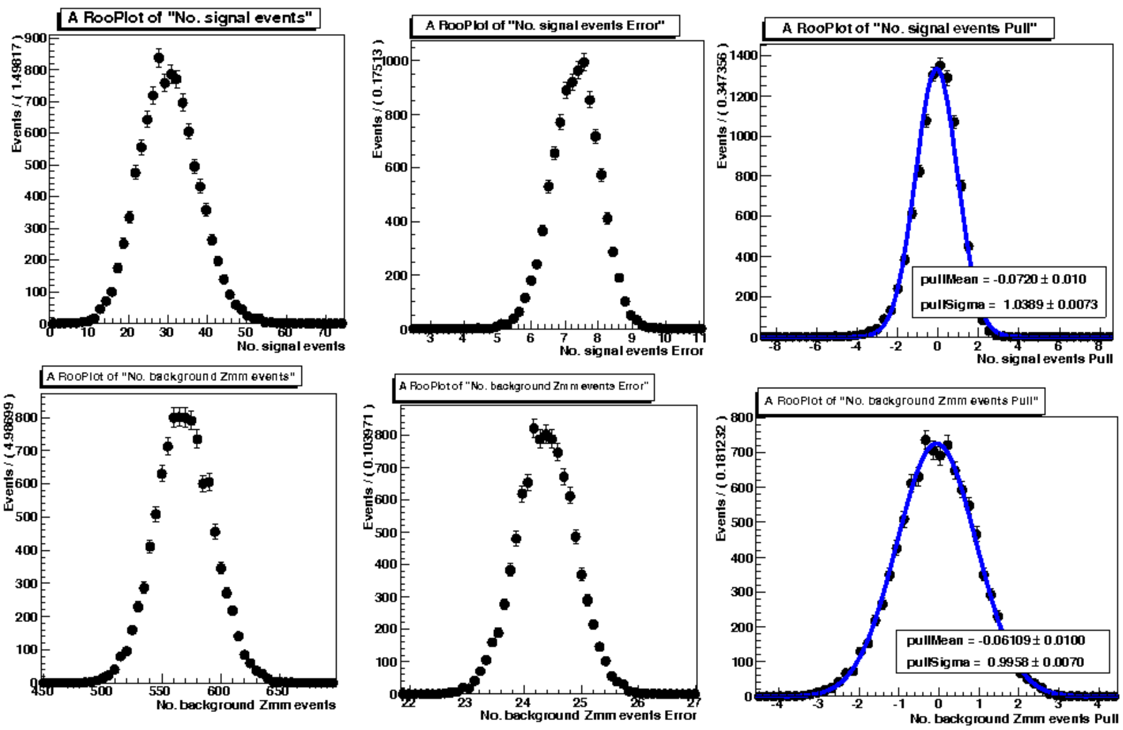

(a) Results of running 10000 Pseudoexperiments over generated MC samples.

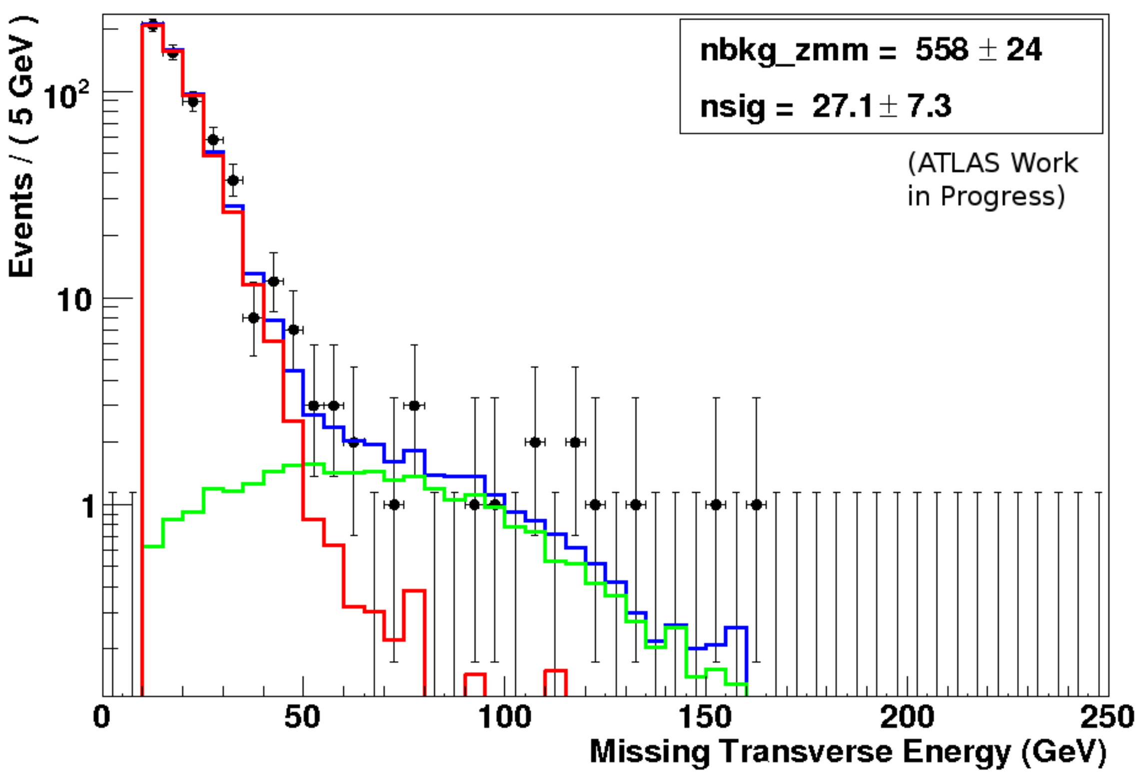

(b) Results of running likelihood fitting macro over 2010-7 TeV data.

Figure 5.1: Attempting a measurement with the missing transverse energy. Here, the Drell-Yan background is shown in **[RED]**, the $t\bar{t}$ signal in **[BLUE]** and the secondary backgrounds in **[GREEN]**.

$\mathcal{L}_{MC}$ correspond to the luminosities of the dataset being examined and the total Monte Carlo sample being used to make the prediction. The additional uncertainties from each sample are summarized in table 5.2, and collectively contribute an additional uncertainty of ±3 pb.

Table 5.2: Contributions to statistical uncertainty from secondary backgrounds held fixed in the fitting algorithm, for $\mathcal{L} = 32.1$ pb^{-1}. The collective statistical uncertainty contributed by these background sample is $\Delta N = 1.66$ events (±3 pb).

Sample		N'	$\mathcal{L}_{MC}$(pb^{-1})	ΔN
Single Top	Wt_McAtNlo	42	910.5685	0.22846
Diboson ZZ	ZZinclNp0	754	16724.6629	0.05270
	ZZinclNp1	451	16528.9256	0.041243
	ZZinclNp2	716	46891.4350	0.01831
	ZZinclNp3	379	737308.14640	0.00085
Diboson WW	WWinclNp0	34	20103.3360	0.00931
	WWinclNp1	141	20929.10313	0.01821
	WWinclNp2	561	28102.9216	0.02705
	WWinclNp3	489	46415.6375	0.01529
Diboson WZ	WZinclNp0	797	18668.4756	0.04854
	WZinclNp1	1071	20704.6542	0.05073
	WZinclNp2	621	18679.1818	0.04282
	WZinclNp3	665	44405.9362	0.01864
$Z \to \tau\tau$	ZtautauNp0	1	377.7412	0.08498
	ZtautauNp1	6	388.1487	0.20257
	ZtautauNp2	19	385.3473	0.36310
	ZtautauNp3	4	409.6125	0.15673
	ZtautauNp4	6	423.6857	0.18558
	ZtautauNp5	3	584.3091	0.09515
Sum				**1.6603**
RSS				**0.5601**

5.4 Systematic Uncertainties

Systematic errors will affect the expectation value of each individual measurement in a set, causing a bias throughout the entire experimental dataset. They arise due to many reasons in an experiment: the improper calibration of instruments, slightly varying environmental conditions or errors in observation among others. For example, GPS satellites will return invalid coordinates if they fail to account for the effects of relativity. At a smaller scale, a balance will consistently return invalid masses if it has not been zeroed correctly. Systematics may also arise due to imperfections in theoretical modelling: the natural frequency of a pendulum will suffer a bias if the mass of the string and support are not considered.

In ATLAS, systematics arise from a variety of sources and have been extensively studied by the physics analysis groups, as they have a direct influence on the precision of any analysis that is performed. Systematics may bias both the measured magnitude and the distribution shape of the number of signal events found, the luminosity calculated, and the acceptance.

5.4.1 Jet Energy Scale

In an ideal scenario, each ATLAS calolrimeter cell would read-out the precise energy of particles passing through it. In reality; however, each cell may return an energy value to within a different degree of precision, and must be individually calibrated accordingly to produce the correct measurement. For the EM calorimeter, these adjustments were be made during machine commissioning: a test beam of photons with precisely known energy was directed at each calorimeter cell, and the difference between the actual and measured beam energies factored into the reconstruction software. For the hadronic calorimeter, no such calibration could be made during commissioning. HCal cell clusters are instead calibrated using in-situ methods, using events with either a photon and jet or a pair of jets produced back-to-back. Because the energy of the photon is measured with relative certainty by the EM calorimeter, the energy of the jet may be inferred by the conservation of momentum and used to calibrate the cluster of active HCal cells collectively.

This method of calibration introduces the dominant systematic uncertainty present in top-related physics analysis (among others), known as the jet energy scale (JES).

At present, the average uncertainty introduced to the measurement through the jet energy is 7% [41]. To determine the impact of this uncertainty on the cross-section measurement, the analysis was repeated twice: once with jet energies increased by 7%, and once with energies lowered by 7%. The corresponding cross-section measurements are presented below in table 5.3.

Table 5.3: Results of repeating cross-section measurement to examine the effects of the jet energy scale uncertainty on the missing transverse energy distribution shape.

Jet Energy	N_{sig}	ΔN_{sig}	N_{bg}	ΔN_{bg}	$\sigma_{t\bar{t}}$
High (+7%)	26.5	7.3	658	26	144.45
Low (-7%)	28.9	7.5	471	22	157.53

The corresponding percent uncertainty on the cross-section measurement may be obtained by simply taking the difference between the high and low JES values as

$$\Delta\sigma_{t\bar{t}} = \frac{\sigma_{+7\%} - \sigma_{-7\%}}{\sigma_{t\bar{t}}} \tag{5.7}$$

which yields an uncertainty of $\Delta\sigma_{t\bar{t}} = \pm 0.1\%$ (± 1.5 pb).

5.4.2 Others

Other systematic effects may also bias the measured cross-section, though to a lesser extent than the bias due to the jet-energy scale. Due to their smaller (though not negligible) effect on the measurement, they have not been explicitly considered but are instead briefly discussed below.

Simulation of the lepton trigger, reconstruction and selection algorithms in Monte Carlo samples can result in deviations between the simulated efficiencies and those found in the actual data. These deviations are examined by studying Drell-Yan events selected from the dataset, and are used to compute 'scale factors' which compensate for the differences. These measurements introduce a systematic uncertainty on the acceptance value.

As adjustments were often being made to the operating parameters of the LHC during the period that the 2010 dataset was collected, the instantaneous luminosity varied widely during this time over several orders of magnitude[1]. This means that on average, two additional soft *pp* collisions occurred for each hard *pp* collision recorded by ATLAS. These effects may be compensated for in the MC samples by overlaying a pair of minimum-bias events over each sample event. Analysis involving data samples naturally includes the effects of minimum-bias pileup events, and so the uncertainty resulting from these effects tends to be small: explicit consideration of this systematic was neglected even in the CERN Top-WG analysis [12].

[1]The maximum instantaneous luminosity recorded by ATLAS during the period this data was recorded (the 2010-7 TeV run) was about $2 \times 10^{32}/\ \mathrm{cm}^2\ \mathrm{s}$, on October 25th, 2010 [19].

Chapter 6

Conclusion

A measurement for the $t\bar{t}$ dimuon cross-section in ATLAS was obtained by using a likelihood fit to discern the signal events from various background processes present in the sample, for a dataset of $\mathcal{L} = 32.1$ pb^{-1}. By using the missing transverse energy as the discriminating variable in the fit, a cross-section measurement of

$$\sigma_{t\bar{t}} = 148.8 \pm 39.8\ (Stat.)\ \pm (Syst.)\ \text{pb} \tag{6.1}$$

was obtained, where the first quoted error is statistical and the second is due to the considered systematic uncertainties. Additional systematic uncertainty is present on the measurement, but has not been considered explicitly in this analysis. A summary of the measured $t\bar{t}$ cross-section and the impact from the various sources of uncertainty considered above is presented in table 6.1. These measurements are found to be in agreement with the ATLAS Top-WG dimuon cross-section measurement [12] (based on a data sample of $\mathcal{L}$ =35.3 pb^{-1}) of

$$\sigma_{t\bar{t}} = 194^{+57}_{-51}{}^{+32}_{-20}\ \text{pb} \tag{6.2}$$

where the first reported uncertainty is statistical, and the second systematic.

Table 6.1: Cross-section measurement, with list of contributions to uncertainty from considered sources. In the reported cross-section, the first uncertainty represents the statistical uncertainty in the measurement, and the second represents the systematic. The JES uncertainty reported below considers only uncertainty in the shape of the $\not{E}_T$ distribution due to these effects. Additional systematic uncertainty is present on the measurement which has not been explicitly calculated in this analysis.

$\not{E}_T$	Measured Cross-Section	148.8 pb
	Statistical Uncertainty (from Fit)	±39.8 pb
	Uncertainty from Fixed Backgrounds	± 3 pb
	Jet Energy Scale Uncertainty	± 1.5 pb
	Compiled Measurement:	148.8 ± 39.8 ± 3.35 ± *(Syst.)* pb

From these results, it seems that a likelihood-fitting method is a promising way of separating the signal and background events in a given dataset while maximizing event acceptance, resulting in a measurement with smaller statistical uncertainties than would be obtained from a traditional 'cut and count' analysis performed over the same dataset.

Further work to be done on this project includes a thorough consideration of all background processes to this measurement. One approach to improving the fit's accuracy would be to modify the fitting macro to allow the number of events due to secondary background processes to fluctuate in the fit. An explicit measurement of the contribution from the QCD multijet background also needs to be made: in the ATLAS Top-WG analysis, this background was found to be consistent with 0, though with the looser event selection used in this analysis a confirming measurement is needed. A proper propagation of the systematic uncertainties through the fit also needs to be made, replacing their brief consideration here. Some systematics may have a higher impact in this study than in the ATLAS analysis due to the higher acceptance in this study, though others may have less of an effect due to the data-driven nature of other aspects (in particular, the Drell-Yan background analysis).

Bibliography

[1] J. Terning. Standard Model. CERN, Jul 2010. CERN Summer Students Lectures.

[2] G. Dvali and G. Guidice. Beyond the Standard Model. CERN, Jul 2010. CERN Summer Students Lectures.

[3] Wikipedia. Standard Model — Wikipedia, the free encyclopedia, 2010. [Online; accessed 21-June-2010].

[4] J. H. Christenson, J. W. Cronin, V. L. Fitch, and R. Turlay. Evidence for the 2π Decay of the $k2$ Meson. *Phys. Rev. Lett.*, 13(4):138–140, Jul 1964.

[5] Makoto Kobayashi and Toshihide Maskawa. CP-Violation in the Renormalizable Theory of Weak Interaction. *Progress of Theoretical Physics*, 49(2):652–657, 1973.

[6] H. Harari. A New Quark Model for Hadrons. *Physics Letters B*, 57(3):265 – 269, 1975.

[7] M. L. Perl *et al.* Evidence for Anomalous Lepton Production in $e + -e-$ Annihilation. *Phys. Rev. Lett.*, 35(22):1489–1492, Dec 1975.

[8] F. Abe *et al.* CDF Collaboration. Observation of Top Quark Production in $p\bar{p}$ Collisions with the Collider Detector at Fermilab. *Phys. Rev. Lett.*, 74(14):2626–2631, Apr 1995.

[9] S. Abachi *et al.* DØ Collaboration. Search for High Mass Top Quark Production in $p\bar{p}$ Collisions at $\sqrt{s} = 1.8$ TeV. *Phys. Rev. Lett.*, 74(13):2422–2426, Mar 1995.

[10] C. Amsler *et al.* Particle Data Group. PDGLive Particle Summary. *Review of Particle Physics*, B667(1), 2008.

[11] Dhiman Chakraborty, Jacobo Konigsberg, and David Rainwater. Review of Top Physics. Mar 2003.

[12] Measurement of the top quark pair production cross-section with ATLAS in pp collisions at $\sqrt{s} = 7$ TeV in dilepton final states. Technical Report ATLAS-CONF-2011-034, CERN, Geneva, Mar 2011.

[13] Pran Nath and Brent Nelson *et. al.* The Hunt for New Physics at the LHC.

[14] Tao Han. The "Top Priority" at the LHC. (arXiv:0804.3178. MADPH-08-1509. NSF-KITP-08-55):25 p, Apr 2008.

[15] G Abbiendi. Search for the Standard Model Higgs Boson at LEP. *Phys. Lett. B*, 565(hep-ex/0306033. CERN-EP-2003-011. CERN-L3-271):61–75. 22 p, Mar 2003.

[16] Amos Breskin and Rodiger Voss, editors. *The CERN Large Hadron Collider: Accelerator and Experiments.* CERN, first edition, 2009.

[17] Jean-Luc Caron. Geographic location of CERN. Carte geographique de l'implantation du CERN. AC Collection. Legacy of AC. Pictures from 1992 to 2002., Mar 1998.

[18] CERN. LHC Machine Outreach, 2010. [Online; accessed 15-Jan-2010].

[19] CERN. ATLAS Data Summary, 2010. [Online; accessed 28-June-2010].

[20] Joao Pequenao. Computer Generated Image of the Whole ATLAS Detector. Mar 2008.

[21] Ulrik Egede. *The search for a standard model Higgs at the LHC and electron identification using transition radiation in the ATLAS tracker*. PhD thesis, Lund University, 1998.

[22] ATLAS Collaboration. *Expected Performance of the ATLAS Experiment: Detector, Trigger and Physics*. CERN, Geneva, 2009.

[23] Joao Pequenao. Computer Generated Image of the ATLAS Inner Detector. Mar 2008.

[24] Joao Pequenao. Computer Generated Image of the ATLAS Calorimeter. Mar 2008.

[25] G. Sauvage on behalf of the ATLAS collaboration. The ATLAS electromagnetic calorimeter: construction, comissioning and selected test beam results. *Nuclear Physics B (Proc. Suppl.)*, 150:98–101, 2006.

[26] A. Dotti, A. Lupi, and C. Roda. Results from ATLAS Tile Calorimeter: a comparison between data and Geant4 simulation. *Nuclear Physics B. Proceedings Supplements*, 150:106–109, 2006.

[27] M. Rosvick. TRIUMF HEC Module Manfacturing Procedures. TRIUMF, Feb 1999.

[28] Joao Pequenao. Computer Generated Image of the ATLAS Liquid Argon. Mar 2008.

[29] Joao Pequenao. Computer Generated Image of the ATLAS Muons Subsystem. Mar 2008.

[30] CERN. ATLAS Experiment - What is ATLAS? [Online; accessed 6-July-2010].

[31] H. P. Beck et al. The ATLAS Event Filter. 1999.

[32] S. Ellis. What Is a Jet? CERN, Jul 2010. CERN Summer Students Lectures.

[33] Gerald C. Blazey, Jar R. Dittman, Stephen D. Ellis, V. Daniel Elvira, K. Frame, S. Grinstein, Robert Hirosky, R. Piegaia, H. Schellman, R. Snihur, V. Sorin, and Dieter Zeppenfeld. Run II Jet Physics. 2000.

[34] ATLAS Collaboration. Data-Quality Requirements and Event Cleaning for Jets and Missing Transverse Energy Reconstruction with the ATLAS Detector in Proton-Proton Collisions at a Center-of-Mass Energy of $\sqrt{s}$=7 TeV. Jun 2010.

[35] A. Canepa, J.R. Lessard, I. Nugent, H. Okawa, A. Taffard, and B. Toggerson. Missing Transverse Energy for Top Physics analyses with early ATLAS data at $\sqrt{s}$=7 TeV. ATLAS collaboration, May 2010.

[36] B Acharya, J-F Arguin, M Barisonzi, IM Besana, M Bosman, IC Brock, R Calkins, D Charkaborty, M Cobal, M Cristinziani, J Ferrando, L Fiorini, A Henrichs, B Heinemann, C Helsens, G Khoriauli, T Kuhl, A Juste, T Lari, F Meloni, L Mir, J Nadal, E Nuncio-Quiroz, M Pinamonti, B Radics, U de Sanctis, E Shabalina, L-Y Shan, K Suruliz, DB Ta, C Troncon, and V Vorwerk. Estimation of the W+Jets Background for Top Quark Re-Discovery in the Single Lepton+Jets Channel. Technical Report ATL-COM-PHYS-2010-834, CERN, Geneva, Oct 2010. Supporting document for top paper.

[37] Sidney D. Drell and Tung-Mow Yan. Massive Lepton-Pair Production in Hadron-Hadron Collisions at High Energies. *Phys. Rev. Lett.*, 25(5):316–320, Aug 1970.

[38] J. H. Christenson, G. S. Hicks, L. M. Lederman, P. J. Limon, B. G. Pope, and E. Zavattini. Observation of Massive Muon Pairs in Hadron Collisions. *Phys. Rev. Lett.*, 25(21):1523–1526, Nov 1970.

[39] K Cranmer, M Cristinziani, H Khandanyan, G Lewis, T Liss, A Papadelis, T Poghosyan, D Sherman, J Sjoelin, M Werth, and D Whiteson. Study of

Z/g+jets Background for ttbar to 2 Leptons Analysis. Technical Report ATL-COM-PHYS-2010-845, CERN, Geneva, Oct 2010.

[40] R. J. Barlow. *Statistics: A Guide to the Use of Statistical Methods in the Physical Sciences (Manchester Physics Series)*. WileyBlackwell, reprint edition, 1989.

[41] M Petteni. Setting the ATLAS Jet Energy Scale. Dec 2010.